Nanotechnology **21** (2010) 062001 (20pp) doi:10.1088/0957-4484/21/6/062001

TOPICAL REVIEW

Nanostructured catalysts in fuel cells

Chuan-Jian Zhong[1], **Jin Luo, Bin Fang, Bridgid N Wanjala, Peter N Njoki, Rameshwori Loukrakpam and Jun Yin**

Department of Chemistry, State University of New York at Binghamton, Binghamton, NY 13902, USA

E-mail: cjzhong@binghamton.edu

Received 28 October 2009, in final form 30 November 2009
Published 12 January 2010
Online at stacks.iop.org/Nano/21/062001

Abstract

One of the most important challenges for the ultimate commercialization of fuel cells is the preparation of active, robust, and low-cost catalysts. This review highlights some findings of our investigations in the last few years in developing advanced approaches to nanostructured catalysts that address this challenge. Emphasis is placed on nanoengineering-based fabrication, processing, and characterization of multimetallic nanoparticles with controllable size (1–10 nm), shape, composition (e.g. Ml_nM2_{100-n}, $M1_nM2_mM3_{100-n-m}$, M1@M2, where M (1 or 2) = Pt, Co, Ni, V, Fe, Cu, Pd, W, Ag, Au etc) and morphology (e.g. alloy, core@shell etc). In addition to an overview of the fundamental issues and the recent progress in fuel cell catalysts, results from evaluations of the electrocatalytic performance of nanoengineered catalysts in fuel cell reactions are discussed. This approach differs from other traditional approaches to the preparation of supported catalysts in the ability to control the particle size, composition, phase, and surface properties. An understanding of how the nanoscale properties of the multimetallic nanoparticles differ from their bulk-scale counterparts, and how the interaction between the nanoparticles and the support materials relates to the size sintering or evolution in the thermal activation process, is also discussed. The fact that the bimetallic gold–platinum nanoparticle system displays a single-phase character different from the miscibility gap known for its bulk-scale counterpart serves as an important indication of the nanoscale manipulation of the structural properties, which is useful for refining the design and preparation of the bimetallic catalysts. The insight gained from probing how nanoparticle–nanoparticle and nanoparticle–substrate interactions relate to the size evolution in the activation process of nanoparticles on planar substrates serves as an important guiding principle in the control of nanoparticle sintering on different support materials. The fact that some of the trimetallic nanoparticle catalysts (e.g. PtVFe or PtNiFe) exhibit electrocatalytic activities in fuel cell reactions which are four–five times higher than in pure Pt catalysts constitutes the basis for further exploration of a variety of multimetallic combinations. The fundamental insights into the control of nanoscale alloy, composition, and core–shell structures have important implications in identifying nanostructured fuel cell catalysts with an optimized balance of catalytic activity and stability.

(Some figures in this article are in colour only in the electronic version)

1. Introduction

The reality that fossil fuels are running out and the fact that pollution from using fossil fuels has become an important issue of environmental concern to human health constitute two of the major driving forces for the increasing interest in the development of fuel cells [1]. The auto industry is perhaps the biggest market behind the massive investment in fuel cell development. This is understandable because the price of oil is extremely volatile and has been increasing in

[1] Author to whom any correspondence should be addressed.

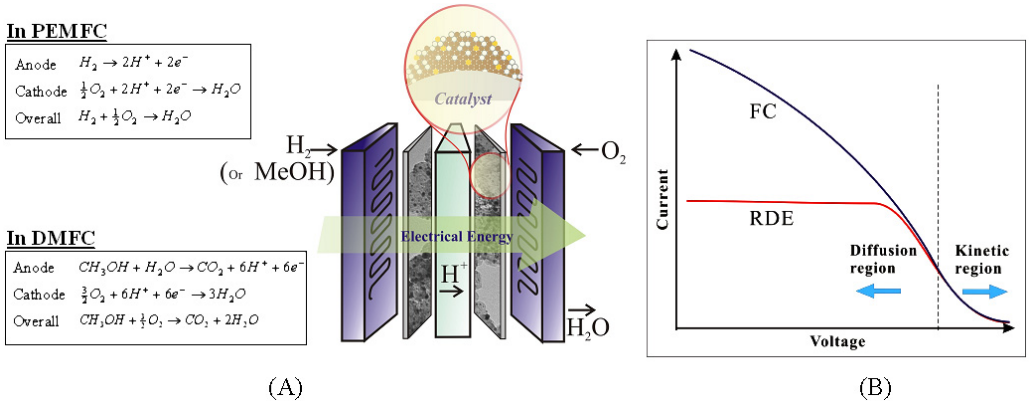

Figure 1. (A) A dissected illustration of the catalysts and the reactions in a fuel cell, e.g. PEMFC or DMFC. (B) A schematic illustration of the different regions of the I–V curves for fuel cell (FC) reactions obtained from measurements of a rotating disk electrode (RDE) in an electrochemical cell and membrane electrode assembly (MEA) in a fuel cell.

the past few years which is likely to continue. Moreover, the harmful emissions of CO_2, CO, SO_2, NO_x, and volatile organic compounds into the atmosphere cause serious environmental damage, increase respiratory problems in humans, and produce 'greenhouse gases' that contribute to global warming. Because fuel cells extract energy from fuel (40–70% efficiency) more effectively than traditional internal combustion engines (∼30% efficiency), this aspect, along with the hydrogen's high efficiency (from 40–70%), could lead to the possibility of better utilization of both heat and electricity in fuel cells and thus make a significant contribution to reducing atmospheric emissions. For example, a fuel cell operating at 60% efficiency would emit 35–60% less CO_2 at the fossil fuel stage and 80% less from hydrogen. This estimate is only based on an efficiency comparison, which does not rule out the consideration of the CO_2 emission from hydrogen generation. In comparison with rechargeable batteries in which the recharge is generally very slow and a fast recharge can damage the performance of the battery, a fuel cell never 'runs down' as long as fuel is present and the recharge of a fuel cell is very fast which does not compromise the performance of the fuel cell. Fuel cells such as proton exchange membrane fuel cells (PEMFCs) and direct methanol fuel cells (DMFCs) become attractive because of high conversion efficiency, low pollution, low weight, high power density, and a wide range of applications from power sources in automobiles and space shuttles to power supplies for electronic devices such as PCs, notebooks, and cellular phones.

Unlike batteries, fuel cells have a constant flow of fresh chemicals into the cell and thus potentially have an unlimited life. A hydrogen PEMFC converts flows of hydrogen and oxygen through a membrane electrode assembly (MEA) into water and produces electricity (figure 1(A)). At the anode, hydrogen is forced through a catalyst where it is ionized. At the cathode, oxygen reacts with the products from the anode (the protons and electrons) to produce water. The net reaction produces electricity and heat, with water as the only product.

The electrochemical reactions occur at the surface of the catalyst at the interface between the electrolyte and the membrane. Hydrogen fed on the anode side of the membrane splits into protons and electrons. Protons travel through the membrane, while the electrons travel through the outside circuit where they perform useful work and return to the cathode side of the membrane. At the catalyst sites of the cathode, oxygen is reduced, which combines with the protons forming water. The net result of these simultaneous reactions is a current of electrons through an external circuit—direct electrical current. At a constant pressure of 1 atmosphere, the maximum available voltage from a fuel cell is determined by the energy differences between the initial state of reactants in the process and the final state, i.e. the Gibbs free energy change (ΔG) in the fuel cell process, which can be calculated from the reaction temperature (T), and from changes in the reaction enthalpy (ΔH) and entropy (ΔS). Under standard conditions, the Gibbs free energy change is given as

$$\Delta G^0 = \Delta H^0 - T\Delta S^0.$$

The maximum cell voltage (E^0), or the theoretical potential of the fuel cell, for the hydrogen/air fuel cell reaction at a specific temperature and pressure is calculated by $E = -\Delta G/nF$, where n is the number of electrons involved in the above reaction, and F is the Faraday constant. Since ΔG^0 ($-237\,340$ J mol^{-1}), n, and F are all known, the theoretical hydrogen/oxygen fuel cell voltage can be calculated. Under standard conditions (1 atmosphere pressure and 298 K), the maximum fuel cell voltage is given as

$$E^0 = \frac{-\Delta G^0}{nF} = 1.23(\text{V}). \quad (1)$$

The theoretical hydrogen/oxygen fuel cell potential is 1.23 V. As temperature rises from room temperature to that of an operating fuel cell (80 °C), the values of ΔH and ΔS change only slightly, and the decrease of the absolute value of ΔG is mainly due to the change in temperature, yielding a cell voltage decrease from 1.23 V at 25 °C to 1.18 V at 80 °C. The fuel cell voltage is in general the summation of the thermodynamic potential E_{Nernst}, the activation overvoltage η_{act} (from both anode and cathode overvoltages, i.e., $\eta_{\text{act(cathode)}} - \eta_{\text{act(anode)}}$), and the ohmic overvoltage η_{ohmic}, which can be expressed as

$$E_{\text{Cell}} = E_{\text{Nernst}} + \eta_{\text{act}} - \eta_{\text{ohmic}}. \quad (2)$$

The thermodynamic potential is governed by the Nernst equation in terms of the ΔE_0 (1.23 V) and the operating concentrations ($P(H_2)$ and $P(O_2)$),

$$E_{\text{Nernst}} = 1.229 - (8.5 \times 10^{-4})(T - 298.15) + (4.308 \times 10^{-5})T[\ln(P_{H2}) + 0.5\ln(P_{O2})]. \quad (3)$$

The activation overvoltage is dependent on the electrode kinetics in terms of current flow and concentration change, which are dependent on overvoltages associated with catalyst activity ($\eta_{\text{act(catalyst)}}$) and concentration polarization ($\eta_{\text{act(conc.)}}$). The overvoltage $\eta_{\text{act(catalyst)}}$ is mainly due to the sluggish activity of the oxygen reduction reaction (ORR), whereas $\eta_{\text{act(conc.)}}$ reflects a combination of reactant and product fluxes through the MEA. The ohmic overvoltage (η_{ohmic}) is due to a combination of resistances from the electron flow, proton flow, electrical contact, and membrane, the latter of which is proportional to the membrane thickness and inversely proportional to the membrane conductivity [2]. For PEMFC, the anode overvoltage is very small when pure hydrogen is used. The major problem is the efficiency losses on the cathode electrode due to sluggish electrode kinetics for the ORR. The above parameters can be assessed from I–V curves of the fuel cell reactions (figure 1(B)). The I–V curves can be obtained from a rotating disk electrode (RDE) and fuel cell MEA measurements. Characteristics from both RDE and MEA measurements are comparable in the kinetic region, but each measurement provides important information on the catalyst performance from different perspectives in terms of activity, stability, and other fuel cell parameters. In the kinetic region, the I–V curves largely overlap between RDE and MEA data because the ORR reactivity is largely determined by the activity of the catalyst. Beyond this region, factors such as diffusion and cell resistance are also playing important roles in the overall performance.

Methanol is another highly attractive fuel in DMFCs as it has a theoretical cell voltage of 1.2 V, and a theoretical energy density of 6094 W h kg^{-1} ($\sim 5x$ that of the best battery couples). The thermodynamic potential of a methanol–air fuel cell is also close to that of the hydrogen–air fuel cell (1.23 V). However, its practical energy density is only 1500–3100 W h kg^{-1} while its operating cell voltage is 0.4 V. Currently, the operation voltages for anode and cathode at 60 °C are 0.3 and 0.7 V, respectively [3]. For a methanol fuel cell, while there is a loss in the cathode side due to methanol crossover from the anode side, the main losses are in the anodic electrode kinetics because the methanol oxidation reaction is very slow.

Among many basic components in a fuel cell, including the gas diffusion electrode, polymer membrane, and catalysts, the catalyst is one of the key components. According to the cost breakdown of fuel cell components [4], the cost of catalysts in manufacturing fuel cells is the highest ($\sim$30%) for small production volume, and remains very high with increasing production volume. Currently, low activity, poor durability, and high cost of the platinum-based anode and cathode catalysts in PEMFCs and DMFCs constitute some of the major barriers to commercialization of fuel cells. The slow electrode kinetics at the cathode for the oxygen reduction reaction in PEMFCs, and at the anode for the methanol oxidation reaction in DMFCs, constitutes a major problem area. The large overpotential for oxygen reduction at the cathode represents a loss of about 20% from the theoretical maximum efficiency for the hydrogen/air fuel cells. Due to the high degree of irreversibility of the oxygen reduction reaction, even under open-circuit conditions, the overpotential at the oxygen electrode in PEMFCs is about 0.2 V. The situation is even worse with the DMFCs. The thermodynamic potential for a DMFC is 1.21 V, which is only 20 mV less than that for the PEMFC. Both the methanol oxidation and oxygen reduction reactions are highly irreversible and thus there is a loss of about 0.2 V at the anode for a DMFC under open-circuit conditions, and an enhanced loss of about 0.1 V at the oxygen electrode because of the crossover of methanol from the anode to the cathode [5].

One of the most important challenges for the ultimate fuel cell commercialization is the preparation of active, robust and low-cost electrocatalysts. The poor activity of the catalysts at the cathode for PEMFCs or at the anode for DMFCs [6–9] leads to a loss of about one-third of the available energy. The propensity of poisoning of Pt by CO species (including trace level CO in reformed hydrogen from methanol, natural gas, or gasoline [10, 11]) is another problem for the extensively studied Pt catalysts. The binary PtRu on carbon support has been studied for decades because of the bifunctional catalytic capability [11–13]. The kinetic limitation of the oxygen reduction at cathode catalysts is another problem for fuel cells operating at low temperature (<100 °C) because the rate of breaking the O=O bonds to form water strongly depends on the degree of its interaction with the adsorption sites of the catalyst, and the competition with other species in the electrolyte (e.g. CH_3OH). Metalloporphyrins [3, 14] and PGM alloys [15] have been used to design catalysts for $4e^-$ reduction of O_2 to water. Many studies focused on understanding the mechanism of oxygen reduction on Pt–Fe, Pt–Ni, and Pt–Co [9], including CO- or methanol-tolerant catalysts [8]. Nanoparticles such as PtBi, PtIn, and PtPb intermetallic phases prepared from bulk melts or by reduction of metal-organic precursors [16] and Ru nanoparticles modified with Pt [17] showed promises for applications in electrocatalytic oxidation of methanol or formic acid. The application of high throughput, combinatorial screening methods to screen a large number of catalysts using an optical fluorescence technique to detect proton production on an array of catalyst inks with different compositions has been successfully demonstrated [18, 19]. Individually addressable array electrodes have been also investigated for rapid screening [20–22]. Recently, simple thermodynamic principles have been proposed as guidelines that assume that one metal breaks the oxygen–oxygen bond of O_2 and the other metal acts to reduce the resulting adsorbed atomic oxygen [23]. The high throughput combinatorial screening of catalysts is very useful for rapid screening, including in our latest work [24]. Because the preparation of fuel cell catalysts has been mostly based on traditional methods such as co-precipitation or impregnation [25–27], little is known about how to optimize size, composition, and morphology of multimetallic catalysts. The knowledge is important since the

nanoscale synergistic effects are expected to be different from their macroscopic counterparts, as supported by examples from studies of bimetallic nanoparticles [28–30].

The ability to harness the large surface area-to-volume ratios and the unique binding sites of nanoparticles constitutes a major driving force in exploring nanotechnology in catalysis. It is the nanoscale size range over which metal particles undergo a transition from atomic to metallic properties that leads to new electronic and catalytic properties. To achieve durable and active catalysts with a low cost, new concepts and strategies must be developed for the creation of size-, composition-, and morphology-controlled multimetallic nanoparticles and catalysts. In contrast to most existing catalyst preparations based on traditional co-precipitation or impregnation methods, the foundation of the nanoengineering of multimetallic alloy catalysts [31–37] has many important attributes in creating a synergistic balance of activity and stability of the catalysts. Nanoscale phenomena differ from bulk counterparts in many significant ways, including the atomic–metallic transition, possible phase-reconstitution, different melting points due to size or alloying effects, and synergistic effects due to modified electronic band structure. The recent studies of nanogold catalysts serve as a best example to illustrate the unique properties displayed by nanoparticles. Despite intensive research into the catalytic activity of gold in a restricted nanoscale size range [38], the catalytic origin of nanosized gold and gold-based bimetallic catalysts remains elusive. Gold–platinum nanoparticles of 2–5 nm diameter present an intriguing system for delineating the correlation in view of recent ability in synthesizing AuPt nanoparticles in a wide range of bimetallic composition [30, 39]. Whether the AuPt nanocrystal core is alloyed or phase-segregated is an important question for the exploitation of catalytic activity of the nanoscale bimetallic catalysts. The single-phase alloy properties were revealed in our x-ray diffraction (XRD) studies [30, 39] for the nanocrystal core, which is in contrast to the miscibility gap known for the bulk counterparts [40]. A synergistic catalytic effect is expected to involve the suppression of adsorbed poisonous species and a change in electronic band structure to modify the strength of the surface adsorption [41]. An understanding of how the bimetallic nanocrystal and surface alloy properties are related to the surface binding and catalytic activities is very important. The recent report [42] on the stabilization of platinum oxygen reduction electrocatalysts using gold clusters demonstrated that Pt catalysts can be stabilized against dissolution by modifying Pt nanoparticles with Au clusters. In view of the strong adsorption of OH forming Pt–OH which causes inhibition of the O_2 reduction, there are several important aspects of the recent progress in understanding the synergistic properties of PtM catalysts in ORR in terms of the role of M (metal) in the adsorption of oxygenated species (e.g. O, OH) [17a, 42, 43]. Indeed, the exploitation of the nanoscale catalytic properties of gold [44–47] and the hydrogenation activity of platinum in bimetallic AuPt nanoparticles has recently received increased interest [48–51].

In the area of ORR by Pt and Pt-based bimetallic catalysts, significant insights have been gained in recent years [24, 48–66], including ORR in acidic [52], and alkaline electrolytes [53, 54]. Ultrafine subnanometer Pt clusters synthesized using a phenylazomethine dendrimer template have recently been shown to exhibit high catalytic activity for ORR [55]. The fundamental relationship in electrocatalytic trends on Pt_3M (M = Ni, Co, Fe, Ti, V) surfaces between the experimentally determined surface electronic structure (the d-band center) and the ORR activity reveals a 'volcano-type' behavior in which the maximum catalytic activity is governed by a balance between adsorption energies of reactive intermediates and surface coverage by spectator (blocking) species [56]. Studies involving model Pt and Pt-bimetallic electrocatalysts also focused on the relation between the energetics of adsorption of intermediates and the reaction kinetics, and surface structure and/or composition [57]. Non-covalent interactions between hydrated alkali metal cations $M + (H_2O)_x$ and adsorbed OH (OH_{ad}) species have recently been found to play an important role in ORR, methanol oxidation reaction (MOR), and hydrogen oxidation reaction (HOR) on platinum surfaces in alkaline electrolytes [58]. In the latest density functional theory (DFT) study of ORR electrocatalysts, Pd or Pt alloyed with early transition metals such as Sc or Y were identified as the most stable Pt- and Pd-based binary alloys, which is supported by electrochemical measurements of the activity of polycrystalline Pt_3Sc and Pt_3Y electrodes showing an enhanced factor of 1.5–1.8 and 6–10, respectively, in comparison with Pt [59]. The near surface chemical compositions of nanoparticle catalysts were recently shown to influence the ORR activity of 'Pt_3Co' nanoparticles in a significant way [60]. The enhanced activity of acid-treated 'Pt_3Co' nanoparticles is attributed to the formation of percolated Pt-rich and Pt-poor regions within individual nanoparticles. High-temperature annealing of acid-treated 'Pt_3Co' is shown to promote ordering of Pt and Co and induces Pt segregation on the (100) surface in the first two to three layers of ordered 'Pt_3Co' nanoparticles. To gain insight into the effects of alloy phase properties, skin metals, lattice parameters, and thermal treatments on the electrocatalytic activity and stability, a recent study of activity–stability relationships of ordered and disordered alloy phases of Pt_3Co electrocatalysts for ORR [61] revealed multiple phases at different temperatures. At 600 °C these phases include a disordered fcc $Pt_{95}Co_5$ phase and an ordered 'fct' (L10) $Pt_{50}Co_{50}$ phase. At 950 °C, a single ordered primitive cubic (L12) Pt_3Co phase is obtained. The ordered alloy phases were not stable due to corrosion and dissolution or phase transformation into a disordered structure. The ordered primitive cubic structure exhibited high resistance to sintering. Pt-rich alloy ('fcc1') phase and ordered 'fct' phase were found to diminish the activity gains. In contrast to the catalyst (60–80 at.% Co) with disordered Pt–Co alloy phases, the Co-rich disordered 'fcc2' phase, which exhibits the largest activity increase, the Pt-rich alloy ('fcc1') phase, and the ordered 'fct' phase were found to diminish the activity gains [62]. $PtCo_3$/C catalysts treated between 350 and 1000 °C under reductive conditions were shown to exhibit partial oxidative leaching of Co, yielding a two-fold increase in mass activity [63]. The particle size remains almost constant until 600 °C, after

which a noticeable particle growth and a broadening of size distribution were observed as a result of the formation of different Pt, Pt–Co, and Co phases, in which the fct- and fcc-PtCo phases exhibit the highest catalytic activities. The activity and stability are closely linked to effects of electronic and geometric parameters such as Pt–Pt distance, metal particle size, and surface structure changes of Pt/C and PtM/C catalysts [64]. For Pt–M/C catalysts, the catalytic activity and stability were classified into four categories according to the chemical nature of M: (1) highly corrosive and highly active (M = Fe, Co, V, and Mn); (2) corrosive and highly active (M = Zn, Cu, Mo, and Ni); (3) stable, but less active (M = Zr, Cr, and Ta); and (4) stable and active (M = W and Ti) [24]. A high throughput combinatorial study [65] of the activity–stability–composition relationships between Pt–M alloys and a Pt standard further showed that PtCo, PtNi, PtZn, and PtCu displayed the highest catalytic activities, but suffered from poor chemical stability in acid electrolytes. PtW, PtTi, and PtSe offered modest catalytic activity improvements and good chemical stabilities. In a number of other studies, the ORR specific activity of Pt and Pt–M catalysts is shown to increase linearly with the decrease of Pt–Pt nearest neighboring distance [66]. The formation of a better Pt–M alloy by heat treatment at >700 °C is shown to decrease the Pt–Pt distance and affects the d-band vacancy of Pt, thus improving the Pt electroactivity. However, the increase in catalyst particle size decreases the active area and thus the catalyst mass activity. The hybridization of the 5d state with empty states above the Fermi level can increase the d-band vacancy of Pt, but the particle size increase diminishes this effect.

While these fundamental insights constitute important guiding principles for the design of Pt and Pt-based bimetallic electrocatalysts, a key challenge to the ultimate commercialization of fuel cells is the development of catalysts which satisfy the three criteria: high activity, high stability, and low cost [1, 18, 67]. This review discusses the recent progress in the development of fuel cell catalysts by focusing on nanoscale design, fabrication, and characterization. Specific examples are from our recent findings in the studies of multimetallic nanoparticles (Ml_nM2_{100-n}, or $M1_nM2_mM3_{100-n-m}$, M1@M2, where M (1 or 2) = Pt, Co, Ni, V, Fe, Cu, Pd, W, Ag, Au etc) with organic monolayer encapsulation for the preparation of fuel cell catalysts [28, 31, 32, 34–36, 68]. In addition to an overview of the general background and fundamental issues in fuel cell catalysis, approaches to molecularly mediated synthesis, processing, and activation of multimetallic nanoparticles and their electrocatalytic performance in fuel cell reactions will be discussed. An understanding of how the interaction between the nanocrystals and the substrate relates to the size sintering or evolution in the activation process on planar substrates will be discussed. The characterization of selected examples of bimetallic and trimetallic nanoparticle catalysts will also be highlighted for gaining fundamental insights into the control of nanoscale alloys, and the composition and core–shell structures of these nanostructured catalysts.

2. Nanoengineered bimetallic/trimetallic catalysts

Traditional approaches to preparing supported nanoparticle catalysts involve co-precipitation, deposition-precipitation, ion-exchange, impregnation, successive reduction, calcination, etc, which have been widely used for preparing noble metal catalysts [69]. While a variety of supported Pt-group binary or ternary catalysts have been prepared by traditional methods [15, 69–75], the ability to control the size and composition is limited due to the propensity of metals to aggregate at the nanoscale. Aggregation of nanoparticles leads to eventual loss of the nanoscale catalytic activity in practical applications. The preparation of nanoparticles capped in monolayers, polymers, or dendrimers is rapidly emerging, demonstrating remarkable parallels to catalytic activities for supported nanoparticles [76–80]. Among many emerging approaches to the preparation of nanoparticles or nanostructures, one particular class of nanoparticles with core–shell type structures is beginning to attract interest for addressing some of the challenges in nanoscale catalyst preparation [81, 82]. The core–shell type nanomaterials can be broadly defined as the core and shell of different materials in close interaction, including inorganic/organic and inorganic/inorganic combinations [76, 81–84]. There has been an increasing number of studies in recent years aimed at synthesizing metal nanoparticles in the presence of organic capping agents [76, 82b, 84, 85, 86, 87, 88].

In contrast to traditional approaches to the preparation of supported catalysts, the molecular encapsulation based synthesis and processing strategy involves a sequence of three steps for the preparation of multimetallic catalysts: (1) chemical synthesis of the metal nanocrystal cores with molecular encapsulation, (2) assembly of the encapsulated nanoparticles on support materials (e.g. carbon powders or carbon nanotubes), and (3) thermal treatment of the supported nanoparticles [32, 89]. Figure 2 depicts the general concept and some examples. Examples described in this review will include gold (Au), gold–platinum (AuPt), platinum–vanadium–iron (PtVFe), and platinum–nickel–iron (PtNiFe) nanoparticles.

Using a modified two-phase method [28, 30, 31, 90], Au or AuPt alloy nanoparticles of 2 nm core size and different compositions encapsulated with organic shells were synthesized by controlling the feed ratios of the two metal precursors (e.g. $AuCl_4^-$ and $PtCl_6^{2-}$) [31]. Bimetallic nanoparticles in which the nanocrystal core consists of one metal core and another metal shell (core@shell) such as Au@Pt and Pt@Au were also synthesized by the seeded growth method [68]. Such nanoparticles were assembled onto carbon black materials, and the carbon-supported nanoparticles were then subjected to thermal treatment under controlled atmosphere which involves the removal of organic shells and calcination of the alloy nanoparticles. The as-synthesized Au_mPt_{100-m} nanoparticles with different compositions are capped with thiol/amine monolayer shells. Varying the feeding ratio of the metal precursors used in the synthesis controls the bimetallic composition and sizes of the nanoparticles.

PtVFe nanoparticles capped with oleylamine/oleic acid monolayers were synthesized in thermal decomposition and

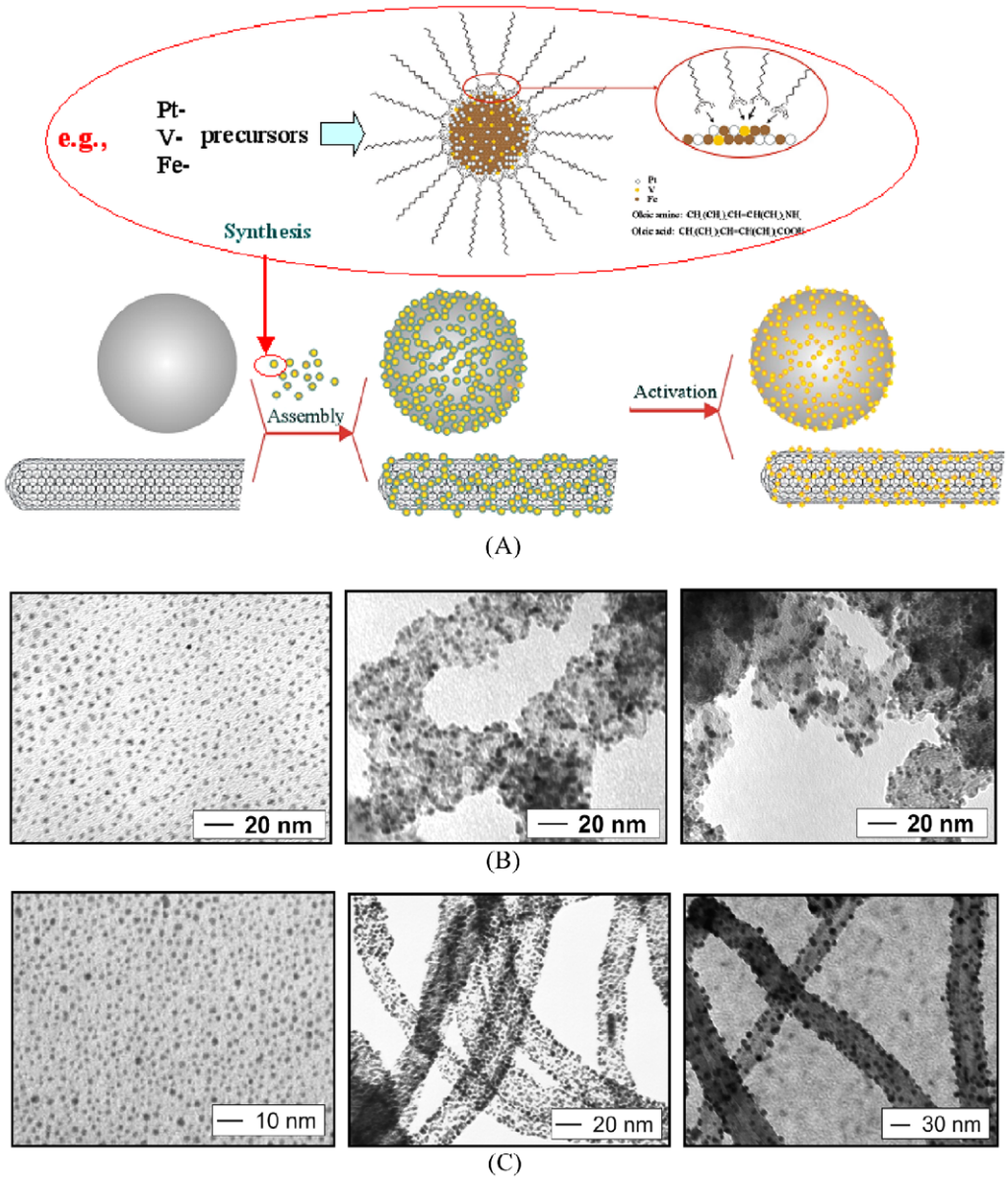

Figure 2. (A) A general scheme showing molecularly engineered synthesis of trimetallic (PtVFe) nanoparticles capped with a monolayer shell of oleic acid/oleylamine, and the preparation of multimetallic nanoparticles (NPs) supported on carbon powders or carbon nanotubes by assembly and activation. (B)–(C) Two sets of TEM images showing $Pt_{19}V_{26}Fe_{55}$ (B) and Au nanoparticles (C) in three stages (from left to right): as-synthesized, assembled on carbon black or carbon nanotubes, and activated (450 °C for B, and 300 °C for C).

reduction reactions by controlled molar ratios of three metal precursors, $Pt^{II}(acac)_2$, $V^{IV}O(acac)_2$, and $Fe^0(CO)_5$ [91]. This method was also applied to the synthesis of PtNiFe nanoparticles. The basic morphology of the observed nanoparticles is largely characterized by the highly faceted nanocrystal feature, which is observable by a close examination of the shapes of the individual nanocrystals. The particles are highly monodispersed, with an average size of 1.9 ± 0.3 nm. The fact that the nanoparticles have well-defined interparticle spacing and display domains of hexagonal ordering is indicative of the encapsulation of the nanocrystal cores by organic monolayers. While the sizes of the ternary nanoparticles varied slightly depending on the actual composition, the data demonstrated the monodispersity of the size. Nanoparticles with average diameters ranging from 1.4 to 3.2 nm have been obtained, with size monodispersity in most cases ranging from ±0.2 to ±0.6 nm.

Molecularly mediated assembly (and/or dispersion) of the capped metal or alloy nanoparticles on planar [92, 93] and carbon nanomaterials (carbon black, e.g. Vulcan XC-72R) [28, 92b] and nanotubes (CNT, 20–60 nm diameters) [89] exploit the interparticle and particle–support interactions such as van der Waals, hydrogen and covalent bonding. Examples of the mediator/linker molecules include 1,9-nonanedithiol (NDT) and 11-mercaptoundecanoic acid (MUA). The assembled particles are highly dispersed and the sizes remain unchanged. The loading of nanoparticles on carbon can be controlled effectively by manipulating the carbon-to-particle ratio and the solvent properties. The metal loading can be determined by thermogravimetric

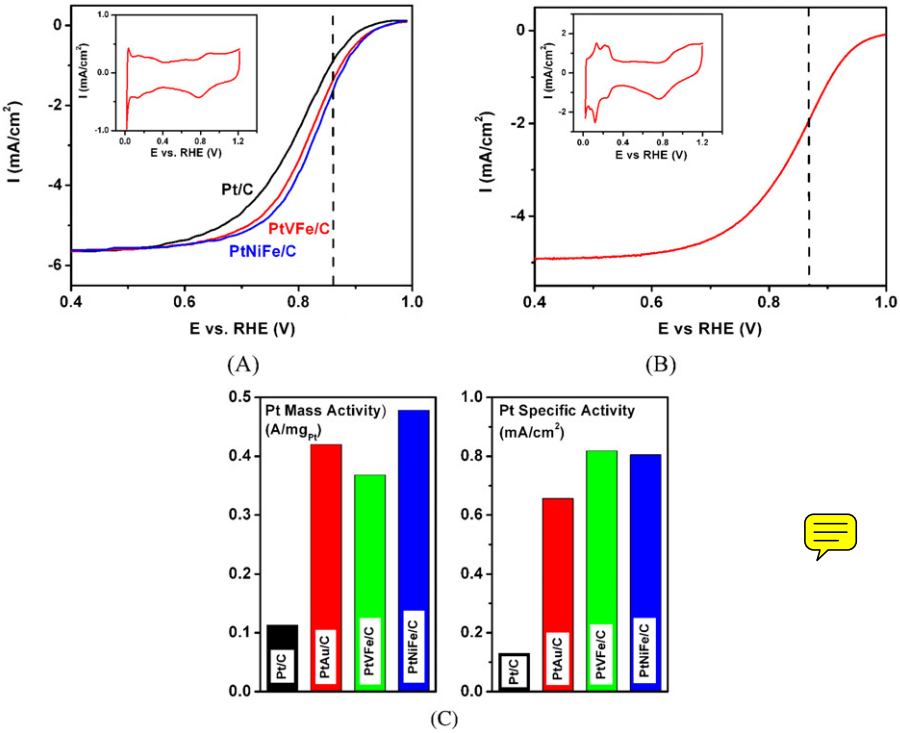

Figure 3. Electrocatalytic activities for ORR based on RDE measurements. (A) RDE curves for $Pt_{32}V_{14}Fe_{54}$/C (31% metal loading) and $Pt_{31}Ni_{34}Fe_{35}$/C (30% metal loading) in comparison with standard Pt/C (36% metal loading) catalysts on a glassy carbon electrode (catalyst loading 15 μg, 0.196 cm^2 geometric area) in 0.5 M H_2SO_4. (5 mV s^{-1}, 2000 rpm). (B) RDE curve for alloy $Au_{23}Pt_{77}$/C (15%Pt) in 0.5 M H_2SO_4. (10 mV s^{-1}, 1600 rpm). (Insets in (A) and (B): cyclic voltammetric curves for determining electrochemical active areas (ECA).) (C) Comparison of mass activities and specific activities for carbon-supported monometallic, bimetallic, and trimetallic catalysts ($E = 0.858$ V versus RHE).

analysis (TGA) and direct current plasma-atomic emission spectroscopy (DCP-AES) techniques. The use of CNTs as support materials is expected to provide both large surface area and increased accessibility due to the high rigidity. CNTs have in recent years stimulated extensive research on the properties of nanometer-scale networks and catalysis [94] for hydrogen storage materials and in fuel cells. Filling metal nanoparticles inside carbon nanotubes is elegantly demonstrated for electrocatalytic methanol oxidation and oxygen reduction [95]. The carbon-supported nanoparticle catalysts can be activated by thermal treatment in a tube-furnace under controlled temperatures and atmosphere including oxidative (in air), reductive (in H_2), and inert (N_2) conditions. The activation and calcination involves: (1) removal of the surface capping agents, and (2) possible reconstitution of the nanocrystal composition or change in morphology. The key is to control the size and composition. The calcination treatment is well documented for catalyst preparations, including surfactant-capped Pt/Ru [82b], PtFe [87], core–shell Pt/Ru [96], and metal-carboxylate linked Au [97] nanoparticles. The surface mobility and adhesion of metals on the support materials depends on surface composition and surface interactions, as demonstrated for strong adhesion support materials (e.g. TiO_2) [98, 99]. Examples to show electrocatalytic activities of the activated catalysts for ORR involved both RDE and FC performance measurements.

Combinatorial studies of a series of Pt-based bimetallic alloy thin film catalysts have revealed significant increase of activities for the oxygen reduction reaction with certain bimetallic catalysts (e.g. PtFe, PtNi, and PtV thin films) [24]. The introduction of a third metal to the alloy is expected to produce a combination of effects such as the reduction of the Pt–Pt lattice distance, the addition of surface sites for the formation of metal–oxygen bonds and adsorption of OH^-, and the modification of the d-band center. Among the various carbon-supported trimetallic nanoparticle catalysts, PtVFe/C and PtNiFe/C alloy nanoparticle catalysts were shown to be highly active for ORR [32]. Figures 3(A) and (B) show a representative set of RDE polarization curves for ORR at $Pt_{32}V_{14}Fe_{54}$/C and $Pt_{31}Ni_{34}Fe_{35}$/C catalysts, and for an alloy $Au_{23}Pt_{77}$/C catalyst.

The current extracted from the kinetic region in the RDE curve, together with the Pt loading in the catalysts, provides a measure of the mass activity (MA (A/mg_{Pt})). The voltammetric currents in the hydrogen adsorption/desorption region (0–0.4 V) are characteristic of Pt on the nanocrystal surfaces accessible to oxygen in the electrolyte (see insets in figures 3(A) and (B)). The integration of the current flow in this region provides a measure of the electrochemical active area (ECA), from which Pt-specific activity (SA (mA cm^{-2})) can be determined. In figure 3(C), the mass activities and specific activities are compared for several carbon-supported monometallic, bimetallic, and trimetallic catalysts. The PtVFe/C and PtNiFe/C catalysts were shown to exhibit a three–five fold increase in mass activity and a seven–eight fold increase in specific activity in comparison with commercially

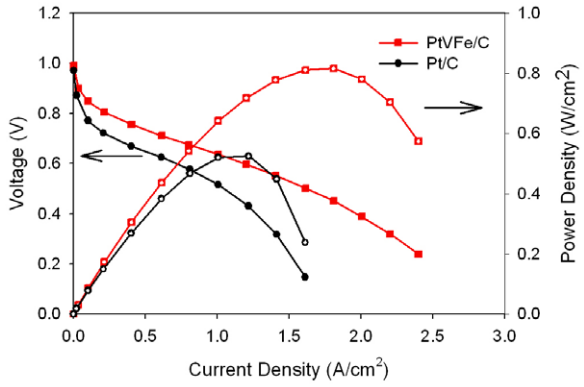

Figure 4. Polarization (closed symbols) and power density (open symbols) curves of MEAs with $Pt_{42}V_{19}Fe_{39}$/C (squares), or Pt/C (circles), as cathode catalysts in a PEMFC at 75 °C [101]. $Pt_{42}V_{19}Fe_{39}$/C catalyst (21% metal loading, 0.4 mg_{Pt} cm^{-2}) was used for the cathode and Pt/C catalyst (20% Pt/C (E-tek), 0.4 mg_{Pt} cm^{-2}) for the anode. Reprinted from [101] with permission from Elsevier.

available Pt catalysts under similar loading and test conditions. For AuPt catalysts, the ORR mass activities were found to be strongly dependent not only on the bimetallic composition (Au_mPt_{100-m}), but also on the nature of the electrolyte [31]. The strong dependence of the mass activity on the bimetallic composition in the alkaline electrolyte was evidenced by the exhibition of a maximum in the composition region of 60–80%Au, which is higher than those for Pt/C and Au/C by a factor of 2–3. In acidic electrolyte, our recent work has shown that an alloyed $Au_{23}Pt_{77}$/C (15%Pt) catalyst exhibited mass activity and specific activity larger than a Pt/C catalyst by a factor of 4–5 [100]. The increases in mass activity and specific activity for these and other trimetallic and bimetallic nanoparticle catalysts ($M1_nM2_{100-n}$, or $M1_nM2_mM3_{100-n-m}$) [100] demonstrated the effectiveness of the alloy composition in enhancing the electrocatalytic performance.

Electrocatalytic performance evaluation of the catalysts in actual fuel cells has recently begun for assessing the viability of the nanoengineered catalysts for practical application in PEMFCs [101]. One example involved the evaluation of PtVFe/C catalysts [101]. The MEA was fabricated using catalyst-Nafion ink painted on a carbon paper. As shown in figure 4 for a set of fuel cell performance data comparing $Pt_{42}V_{19}Fe_{39}$/C and Pt/C catalysts under the loading condition of 0.4 mg_{Pt} cm^{-2}, both the cell voltage and the power density for the fuel cell with PtVFe/C catalyst in the cathode are found to be much higher than those for the Pt/C catalyst under the same test conditions.

The FC performance data are compared in terms of the polarization curve and power density between the $Pt_{42}V_{19}Fe_{39}$/C and the Pt/C catalysts. In comparison with the peak power density of Pt/C (1.22 A cm^{-2} and 0.52 W cm^{-2} at 0.43 V), values of 1.81 A cm^{-2} and 0.82 W cm^{-2} at 0.45 V were found for the PtVFe/C catalyst. The fuel cell with a PtVFe/C catalyst showed a 50% increase in peak power density in comparison with that of Pt/C. These results demonstrate that the trimetallic nanoparticle catalyst has a much better fuel cell performance than a Pt/C catalyst, which is consistent with the electrocatalytic activity trend revealed by the RDE data.

The stability of the PtVFe/C catalysts was also evaluated by both RDE and MEA FC measurements [101]. In RDE measurements, the stability was evaluated by comparing the electrocatalytic activities between fresh catalysts and catalysts after extensive electrochemical cycling in the reaction potential window. For example, the current of the PtVFe/catalysts before and after 5000 cycles showed no indication of any noticeable decrease in the kinetic region. The stability of the trimetallic catalysts was also examined under the fuel cell testing condition by holding the current at 700 mA cm^{-2}. Again, the fuel cell showed no indication of decrease in cell voltage over a 10 day period. While a further long-term durability test is needed for a complete assessment of the catalyst stability, the RDE and MEA FC test results showed that the trimetallic catalysts have promising applications in PEM fuel cells.

3. Probing activation of the nanostructured catalysts

The understanding of the size, shape, and composition evolution in the activation process is important for the control. The thermal activation of a core–shell type nanoparticle assembly on a planar substrate surface has been studied as a model system (figure 5).

Theoretically, thermally induced sintering or coagulation occurs by either sintering of small particles into larger-sized particles or agglomeration of small particles into a coagulating cluster [98]. The driving force for sintering can be described by a basic Gibbs–Thompson (GT) relation,

$$\mu(r) - \mu(\infty) = 2\gamma\Omega/r$$

where γ represents surface free energy of the metal, and Ω represents the bulk metal volume per atom. This equation relates the difference between the chemical potential of a metal atom in a particle of radius r, and that in the bulk. Recent model studies [99] demonstrated that the dependence of this energy on particle size is much stronger than predicted. There are essentially two limiting mechanisms [98b]: diffusion of intact particles followed by coalescence, and detachment of atoms from smaller particles followed by diffusion across terraces and reattachment to larger particles. Currently little is known about how surface capping (surface tension) and wettability or adhesion (surface diffusion of metals) affect the sintering process. Our simulation work is based on the model modified by Campbell *et al* [99],

$$\mathrm{d}r/\mathrm{d}t = [2\gamma\Omega K/(kTr^2)](\mathrm{e}^{-E_{\mathrm{tot}}/kT})[r/r^* - 1]$$
$$\text{where } E_{\mathrm{tot}} = \Delta H_{\mathrm{sub}} - (E_{\mathrm{ad}}^{\mathrm{support}} - E_{\mathrm{diff}}^{\mathrm{support}}) \quad (4)$$

T: temperature of substrate; γ: surface free energy of the metal; Ω: bulk metal volume per atom, $r^* = 1/(\text{average of } 1/r)$; $K = [(2\sin\theta)(\nu_P)(\Omega)]/[(2 - 3\cos\theta + \cos^3\theta)(a)]$ (θ: equilibrium contact angle of the metal particles with the support surface; ν_P: pre-factor in the rate constant for a metal monomer diffusing along the edge of a particle; a: inter-atomic spacing; ΔH_{sub}: metal's bulk sublimation enthalpy; $E_{\mathrm{ad}}^{\mathrm{support}}$: activation energy for adsorption on support;

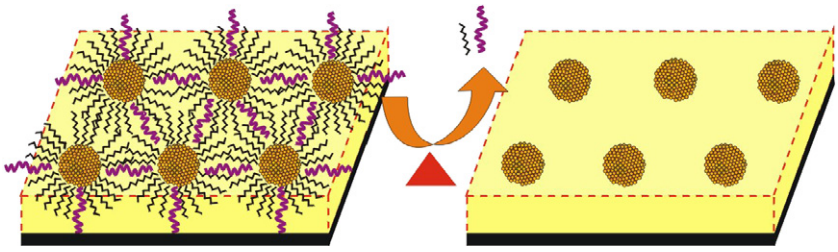

Figure 5. An idealized illustration of the thermal activation of a thin film assembly of nanoparticles with capping/linking molecules on a planar substrate.

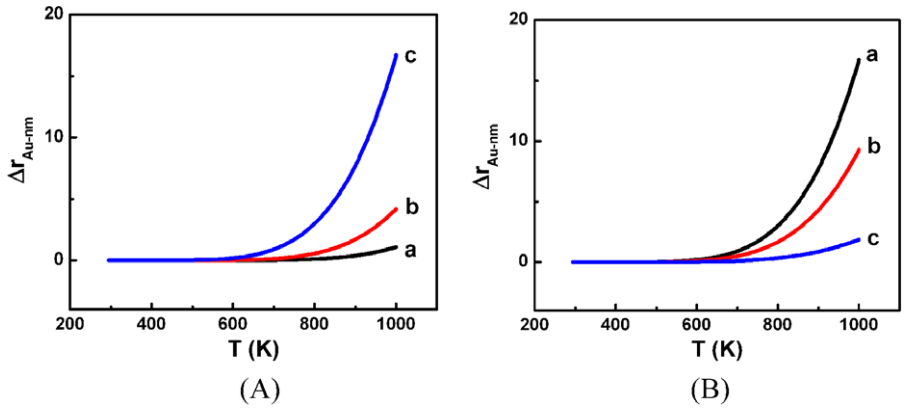

Figure 6. Simulation results for the relative change in average radius of Au nanoparticles versus calcination temperature based on equation (2). (A) at constant γ, different E_{tot}. (B) at constant E_{tot}, different γ. ((A): $\gamma = 0.9$ J m^{-2}; $E_{tot} = 70$ (a), 60 (b), and 50 kJ mol^{-1} (c). (B): $E_{tot} = 50$ kJ mol^{-1}; $\gamma = 90$ (a), 50 (b), and 10 μm^2 (c)). Using $\theta = 90°$, $\nu_P = 4 \times 10^{12}$ s^{-1}, heating rate $= 1$ K s^{-1}, and ΔH_{sub}(for Au) $= 368$ kJ mol^{-1}, a set of simulation results for the relative change in average radius of the Au nanoparticles (for an initial $r = 1$ nm) on a flat substrate as a function of the temperature).

$E_{diff}^{support}$: activation energy for diffusion on support). The rate for the change of a particle's radius (r) is a function of the apparent activation energy E_{tot} [99]. As shown by the simulation results for the relative change in r for Au nanoparticles (initial $r = 1$ nm) on a flat substrate as a function of temperature (figure 6) [92d], the rate for the change of particle size with temperature at constant γ is increased with decreasing E_{tot} (figure 6(A)), whereas the rate at constant E_{tot} is increased with increasing γ (figure 6(B)).

An understanding of how the adsorption energy depends on the interaction of a monolayer-capped nanoparticle with the substrate and the diffusion energy is crucial—the interaction between the nanocrystals and the substrate is important for developing ways to manipulate the surface free energy, wettability, or adhesion, and ultimately the particle sizes. Parameters such as γ, $E_{ad}^{support}$, and $E_{diff}^{support}$ are related to the functional groups of the capping or linking agents, the hydrophobicity, or the binding properties of the substrate, which can be manipulated by changing the functional groups of the capping or interparticle-linking agents. For example, NDT and MUA linked particles could produce acid and methyl (and methylene) at the interfaces, which may affect the initial aggregation of the nanoparticles through energetic contributions from both shell–substrate interaction and Au–substrate interactions. In addition to the correlation of interparticle sintering with particle size and composition, solid-state diffusion on surfaces is one of the mechanisms involved in the calcination-induced size evolution. Atomic force microscopy (AFM) was used to probe the evolution of the morphology of nanoparticles assembled on planar substrates of different wettability (e.g. carbon, graphite, mica, silica, etc). Although AFM cannot resolve well particles of a few nm sizes in the xy plane, the capability of probing spatial morphology and its 0.1 nm resolution in the z-axis enables one to extract useful information [92a, 92d].

The capping/linking molecular shells can be removed by electrochemical [93] and thermal [31, 32, 92] activation treatments. In the case of thermal activation, heating of the nanoparticles under ambient conditions in the temperature range of 200–300 °C can effectively remove the shell/linking materials, as evidenced by TGA curve for decanethiolate (DT)-capped Au_{2-nm} particles (figure 7(A)). The mass decrease starts at about 140 °C and shows a transition at 225 °C. The overall mass change (25 wt%) is consistent with the expectation based on a model calculation of the percentage of the organic shell (26 wt%) [102]. Based on the TGA data, two extremes of the nanostructure can be hypothesized upon thermal activation near the transition temperature. One involves partially capped nanoparticles with intact core size and interparticle space, and the other, naked nanoparticles with controllable larger core size. The interaction of the shell-opened nanocrystals with the substrate surface thus plays an important role in the mobility and the eventual morphology of the nanoparticles. The AFM images described next provided important insight into this hypothesis.

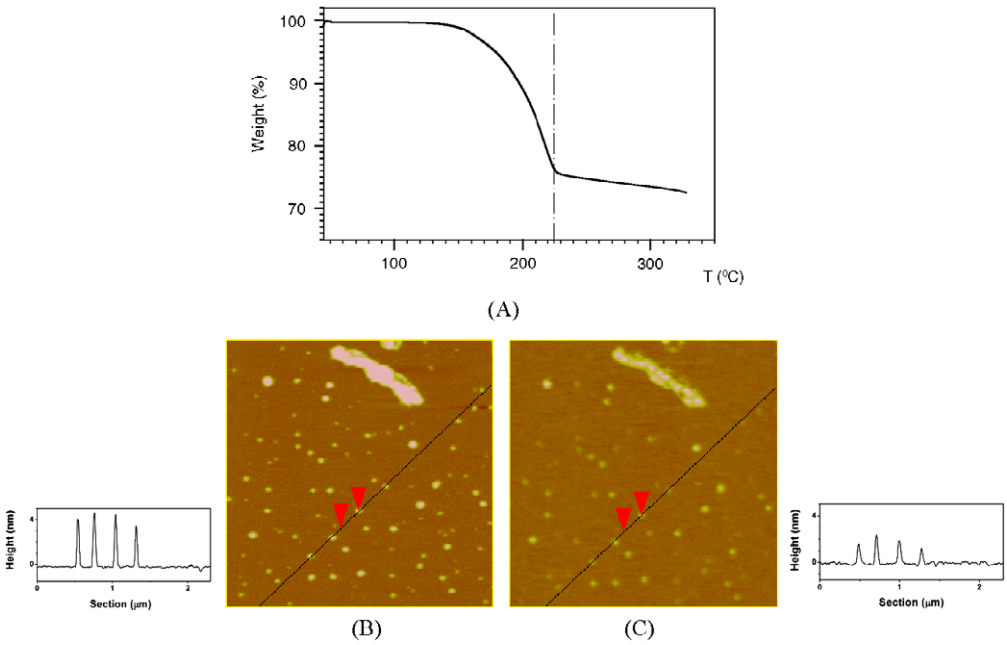

Figure 7. (A) TGA curve of DT/Au_{2-nm} nanoparticles. (B)–(C) *In situ* AFM images ($2 \times 2\ \mu m^2$) for DT-capped Au_{2-nm} on mica before (B) and after (C) thermal treatment at 225 °C for 30 min (image acquired after cooling to room temperature). The top bar of nanoparticles serves as an internal location feature. The cross-section view corresponds to the line drawn in the image. Reprinted with permission from [92d]. Copyright 2004 American Chemical Society.

The change in size of individual nanoparticles (e.g. DT-capped Au_{2-nm}) cast on mica as a result of the thermal treatment at 225 °C can be detected by the change in height data of the AFM images (figures 7(B) and (C)). Before heating treatment, the average particle size determined from the cross-section data (height) is consistent with the expectation for the sum of the core diameter (2.0 nm) and the shell molecular length times a factor of two (∼2.5 nm). After the treatment, the relative position of nanoparticles remains unchanged. The particles displayed a clear shrinkage in size as a result of the removal of the capping shell molecules. There is no apparent aggregation of the nanocrystal cores because the particles are widely separated, and the adhesion (adsorption) of nanocrystals to the surface of mica is quite strong.

The tendency of nanoparticles to aggregate depends on the surface properties of the substrate and the interparticle molecular interaction. Effects of the interparticle molecular linkers and the substrates on size changes were considered for the detailed understanding of interparticle size evolution under thermal activation. For the interparticle molecular linkers, an important function is to define part of the interparticle properties for the as-formed nanoparticle assembly. Because the linking/capping molecules are removed by the heat treatment, as evidenced by infrared (IR) and x-ray photoelectron spectroscopy (XPS) studies [92c], the question is whether this initial spatial definition has any impact on the evolution of nanoparticles. As shown in figure 8 for an NDT-Au_{2-nm} film with a sub-monolayer coverage on mica before and after the treatment at 225 °C for 30 min, the assembled particles are clustered into wire or chain-like morphologies. The cross-sectional data suggest that the nanoparticles form layers that are ∼3 nanoparticles thick on average. After the treatment, the edges of individual particles are better resolved, and the chain-like interparticle morphology remains intact. The removal of the thiolate shell at this temperature was supported by the tapping-mode phase imaging data, which reveals that the dark phase contrast that is normally attributed to a 'softer' material is absent for the thermally treated assembly compared to the as-prepared assembly. The height of the corresponding region in topography images, ∼1 nm, is consistent with the thickness of the organic layer. The corresponding phase image was darker than the nanoparticle features as a result of the presence of thiolate chains. The height analysis of the cross-sectional data reveals average particle sizes of 11.1 ± 3.9 and 13.1 ± 3.4 nm, respectively. The small increase in size is believed to be due to localized aggregation largely from overlapping particles. The largely unchanged interparticle spatial feature in the lateral plane demonstrates that the interparticle spatial property can be controlled even if there is a local aggregation from the overlapped nanoparticles, indicating the important role played by the combination of the initial molecular capping/wiring and the subsequent adhesive interaction of the particle to the substrate in the spatial fixation.

As shown by the morphological evolution for an MUA-$Au_{2\ nm}$ film with ∼1 layer thickness (figure 9), the assembled nanoparticles undergo significant local aggregation after the heat treatment, forming individually isolated and larger-sized particles. The resulting particle sizes are relatively monodispersed (average ∼ 8 nm). The dependency of the morphology of both the as-formed films and the thermally evolved particles on the nature of the linking molecules suggests that the interparticle interaction plays an important role in the thermally induced nanostructural evolution process.

For the substrate effect, the examination of the morphology of the nanoparticle assemblies on a hydrophobic

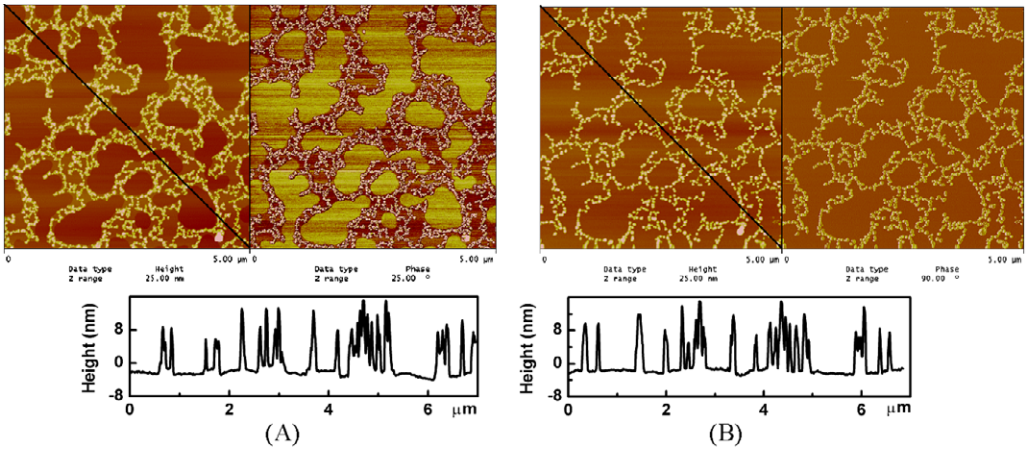

Figure 8. *In situ* AFM images ($5 \times 5\ \mu m^2$, 10 nm/pixel) of an NDT–Au_{2-nm}/mica film before (A) and after (B) heating to 225 °C for 30 min (image was acquired after cooling back to room temperature). In each case, both topography (left) and phase (right) images are included for comparison. The cross-section view corresponds to the line drawn in the topography image. Reprinted with permission from [92d]. Copyright 2004 American Chemical Society.

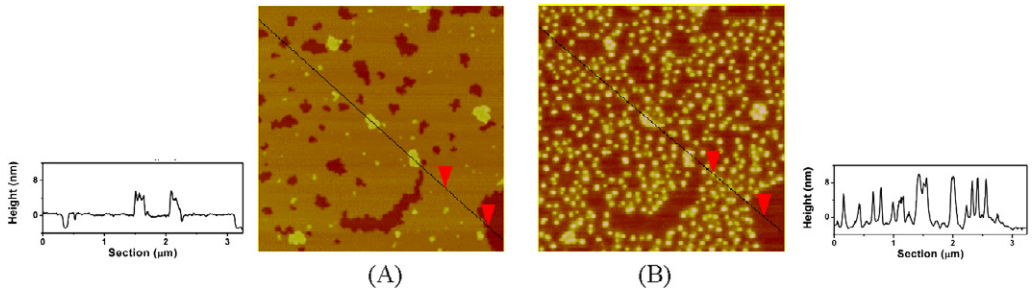

Figure 9. *In situ* AFM images ($2.5 \times 2.5\ \mu m^2$) of an MUA–Au_{2-nm}/mica before (A) and after (B) heating to 225 °C for 5 min. (The image was acquired after cooling back to room temperature.) The cross-sectional view corresponds to the line drawn in the image.

highly oriented pyrolytic graphite (HOPG) substrate before and after heat treatment (figure 10) produced two important findings for the particle evolution. First, the as-formed nanoparticle assemblies (∼2 layers) display relatively uniform coverage on the HOPG surface, in contrast to the formation of domain features on the mica surface. This suggests an important role played by the hydrophobic interaction between the shell/linker component and the substrate. Secondly, the degree of aggregation of the particles after the thermal treatment exhibited several interesting differences between mica and HOPG. In general, the particles on HOPG showed a greater tendency to aggregate than those on mica.

The increase of particle sizes for the MUA linked nanoparticles (average size ∼14 nm) is much larger than the NDT linked assembly (average size ∼10 nm). The observation of particle aggregation both inside and outside the trenches after the thermal treatment suggests that there is a higher surface mobility (or lower particle–substrate interaction) for the assembled particles on the *hydrophobic* HOPG surface in comparison with the *hydrophilic* mica surface. Another intriguing observation is that the nanocrystals are accumulated along step edges of the HOPG substrate after the heating treatment, forming wire-like features. This finding is remarkable because it indicates that the mobility of nanoparticles can be effectively regulated by the step edges on the substrate. Similar phenomena have also been observed for a dendrimer-mediated assembly of Pd nanoparticles on HOPG substrate [103]. A potential application of such a step-edge-guided nanoparticle movement on the surface is the formation of nanowires and other nanoscale shapes on surfaces that can be intentionally engineered (e.g. patterning).

The experimental and theoretical results can be understood based on comparisons of the relative activation energies (E_{tot}(mica) > E_{tot} (HOPG)) and surface tensions ($\gamma(-CH_3)$(mica) < $\gamma(-CO_2H)$ (HOPG)). Based on the theoretical simulation and the qualitative analysis of equation (4), the initial aggregation of the nanoparticles was considered to involve energetic contributions from both shell–substrate interaction and Au–substrate interactions. The basic assumption in our assessment is that the adsorption energy is mainly dictated by the interaction of the monolayer-capped nanoparticle with the substrate, whereas the diffusion energy is largely determined by the interaction of gold nanocrystals with the substrate. This qualitative assumption is reasonable in view of our thermal treatment condition near the organic-removal temperature (∼225 °C), below which the organic shell is partially present and above which the shell is absent and aggregation occurs. The difference between $E_{tot}^{(HOPG)}$ and $E_{tot}^{(Mica)}$ (from equation (4)) can be written as

$$E_{tot}^{(HOPG)} - E_{tot}^{(Mica)} = [\Delta H_{sub}^{(HOPG)} - \Delta H_{sub}^{(Mica)}] - [(E_{ad}^{(HOPG)} - E_{diff}^{(HOPG)}) - (E_{ad}^{(Mica)} - E_{diff}^{(Mica)})]. \quad (5)$$

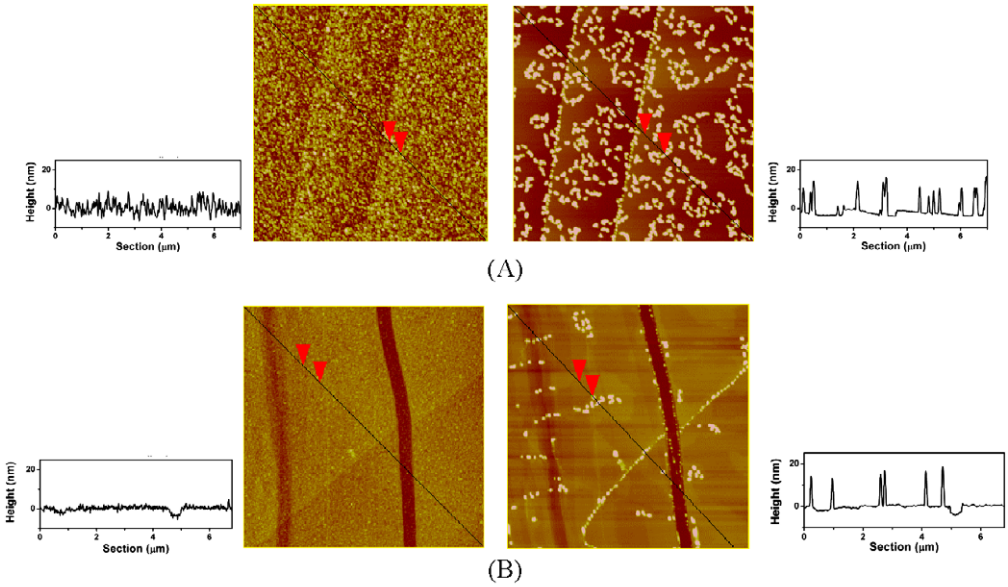

Figure 10. *In situ* AFM images ($5 \times 5\ \mu m^2$) of the thin films on HOPG before (left image) and after (right image) thermal treatment (225 °C, 5 min) for (A) NDT–Au_{2-nm}, and (B) MUA–Au_{2-nm}. Cross-section views correspond to the line drawn in the image. Reprinted with permission from [92d]. Copyright 2004 American Chemical Society.

Since the bulk sublimation enthalpy should not be affected by the substrate in any significant way, we have,

$$E_{tot}^{(HOPG)} - E_{tot}^{(Mica)} = -[(E_{ad}^{(HOPG)} - E_{diff}^{(HOPG)}) - (E_{ad}^{(Mica)} - E_{diff}^{(Mica)})]. \quad (6)$$

The previous work [99] has indicated $E_{ad} - E_{diff} > 0$. Based on the nature of the nanoparticle–substrate adsorption, i.e. the predominant hydrophobic–hydrophobic interaction for the adsorption on HOPG and hydrophobic–hydrophilic interaction for that on mica, it is evident that $E_{ad}^{(HOPG)} > E_{ad}^{(Mica)}$. On the other hand, the reversal of the interaction nature for the diffusion property should lead to $E_{diff}^{(HOPG)} < E_{diff}^{(Mica)}$. Qualitatively, $E_{tot}^{(HOPG)} - E_{tot}^{(Mica)} < 0$, i.e. $E_{tot}^{(HOPG)} < E_{tot}^{(Mica)}$. As such, the particle size on HOPG would increase more significantly than on mica with increasing temperature. For the same HOPG substrate (constant E_{tot} for Au on HOPG), the initial surface tension is larger for MUA linked particles than for NDT linked particles because of $\gamma(-CO_2H) > \gamma(-CH_3)$ [104]. In this case, the particle size increases more significantly for MUA linked particles according to figure 6(B). This is indeed in qualitative agreement with the AFM finding showing larger particle sizes for MUA-Au_{2-nm} on HOPG. These findings are significant because they suggest that the manipulation of the surface free energy, wettability, or adhesion can have an impact on the final size of the thermally processed nanoparticles on the surface. An in-depth correlation of the thermally induced morphological evolution of the nanoparticles with surface energy, surface mobility, and molecular interactions will be useful for exploring their applications in catalysis and electrocatalysis.

The question on how the morphology changes in electrochemically induced catalytic activation [93] was also probed by *in situ* AFM imaging. In this case a nanoparticle-patterned substrate was used as the imaging platform. Such a platform has been demonstrated for probing pH-tuned nanostructural changes [105]. As shown in figure 11(A), a film of MUA linked 5 nm Au particles capped with decanethiolate monolayers was first patterned onto a flat surface of conductive material which forms grids surrounding the $2 \times 2\ \mu m^2$ squares. The morphological changes of the thin film pattern as a result of desorption of the capping/linking molecules from the metal nanoparticles in an electrochemical activation process (e.g. by cycling the potential between 0 and +850 mV in 0.5 M KOH/3M MeOH) can be detected directly by topographical imaging with the empty square as an internal standard. As evidenced by the change in the cross-section views for such a sample after partial desorption of the capping/linking molecules (figure 11(B)), a subtle shrinkage of the void square (x- or y-axis) and a clear increase of the grid height (z-axis) by 10–15% after are detectable in the electrochemical activation. These changes reflected an influx of ions/solvents from the solution into the partially activated film. This demonstration is significant in two ways. First, it shows the viability of probing morphological change upon electrochemical activation in real time. Second, it illustrates the feasibility of developing a technique for screening catalysts in terms of morphological properties.

The detailed *in situ* AFM-detected morphological changes before and after catalytic activation can also be correlated with *in situ* electrochemical quartz crystal nanobalance (EQCN) detected mass changes, which provided information for understanding the surface removal of organic components, reconstitution, and nanocrystal spatial properties in the electrochemical activation process [93c].

4. Probing nanoscale alloys, and the composition and core–shell structures of the catalysts

Examples, including bimetallic AuPt alloy, trimetallic PtVFe or PtNiFe, and core–shell (Au@Pt) nanoparticle catalysts,

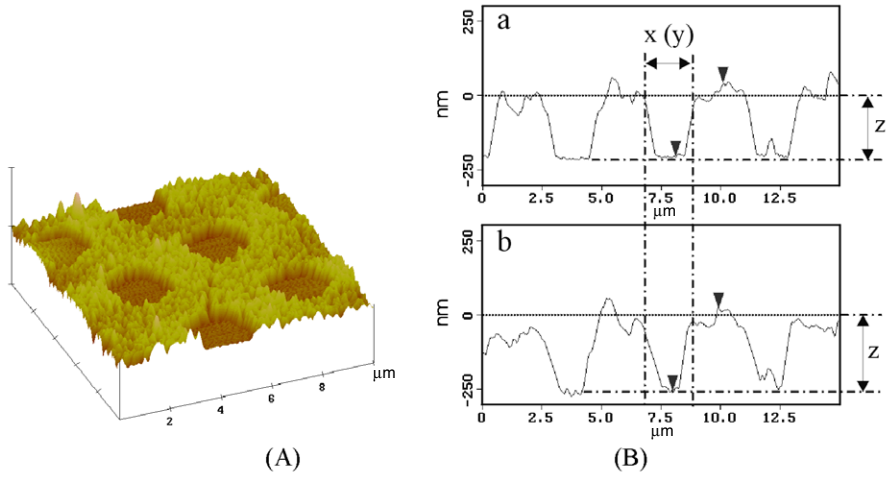

Figure 11. (A) AFM image of mercaptoundecanoic acid linked Au_{5-nm} film patterned on an HOPG substrate. (B) Cross-section views from *in situ* AFM imaging data before ((a) (top), $z = 249$ nm) and after ((b) (bottom), $z = 279$ nm) electrochemical partial activation (i.e. partial desorption of the capping/linking molecules in one cycle between 0 and +850 mV versus Ag/AgCl, saturated KCl) in 0.5 M KOH solution with 3 M MeOH.

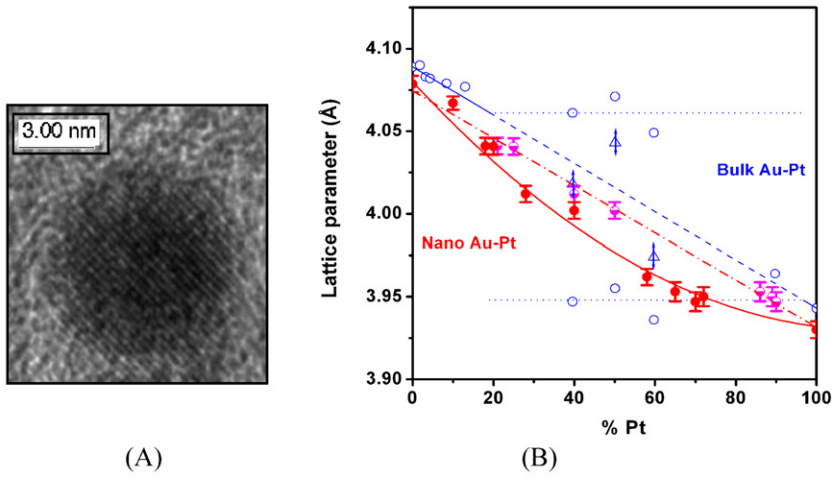

Figure 12. (A) HRTEM of thermally treated AuPt/C catalysts ($Au_{72}Pt_{28}$/C). (B) The lattice parameters versus Pt% for AuPt nanoparticles (the curved (red) and dash-dot (pink) data points and lines) and for bulk AuPt (the open circle data points and solid-dash lines) (blue). For bulk AuPt, the triangle points (blue) represent those at frozen states. For nanoscale AuPt, the half-filled circle points (pink) represent those using the composition derived from fitting the lattice parameter from XRD data, whereas the filled circled points (red) represent those using the composition derived from DCP analysis [30, 41]. Reprinted from [41] with kind permission from Springer Science + Business Media.

are described here to illustrate how the understanding of the nanoscale engineered materials can advance the development of catalysts. The understanding focuses on the characterization of nanoscale alloys, and the composition and core–shell structures of these catalysts.

Nanoscale alloy. The highly crystalline nature of bimetallic AuPt nanoparticles has been evidenced by high resolution transmission electron microscopy (HRTEM) (figure 12(A)). In contrast to the bulk Au–Pt counterparts which display a miscibility gap between 20% and 90% Au [40], the lattice parameters of the bimetallic AuPt nanoparticles determined from XRD characterization were found to scale linearly with Pt% as in a Vegard's type law typically observed with binary metallic alloys (figure 12(B)), demonstrating the alloy properties for the bimetallic AuPt nanoparticles [30]. The lattice parameters were determined for each AuPt sample by carefully determining the positions of the Bragg peaks in the diffraction patterns. In addition, the values for the lattice parameter of the nanoscale AuPt are all smaller than those for the bulk AuPt. This intriguing phenomenon suggests that nanoparticles have smaller inter-atomic distances than those for the bulk counterparts [41], which was the first example demonstrating that the nanoscale AuPt nanoparticles could exhibit single-phase character and small inter-atomic distances in the entire bimetallic composition range, both of which are in sharp contrast to those known for their bulk counterparts. This finding is in fact supported by a theoretical model study [106], which showed that the nanoscale alloying is thermodynamically favored for AuPt nanoparticles smaller than ∼6 nm because the heat of formation is negative, and by

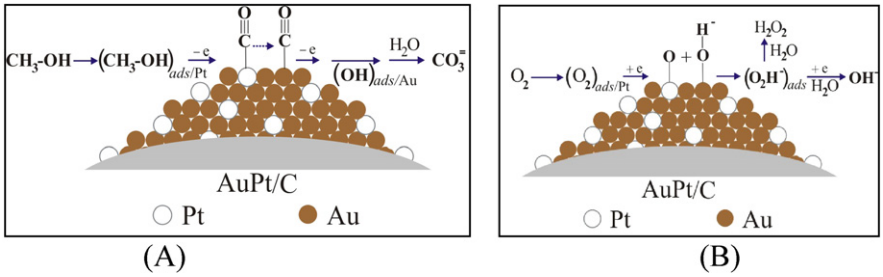

Figure 13. An illustration of possible surface adsorption and reactivity for MOR (A) and ORR (B) on AuPt alloy nanoparticles in an alkaline electrolyte. Reprinted from [41] with kind permission from Springer Science + Business Media, and reprinted from [31a, 39]. Copyright 2006, 2007, with permission from Elsevier.

our recent study of the temperature dependence of the phase properties [100].

The insight into the bimetallic alloy phase also led to the study of surface alloy properties using Fourier transform infrared (FTIR) to probe CO adsorption on AuPt/SiO_2 with a wide range of bimetallic compositions [39, 41]. The CO adsorption on Au-atop sites in a Au-rich surface environment which displays a 2115 cm^{-1} band in the FTIR spectra was found to exhibit a clear trend of diminishing absorbance as Pt concentration increased in the bimetallic catalysts. This band becomes insignificant or even absent at $>\sim$45% Pt. Secondly, the electronic effect of the surface Pt-atop sites alloyed in the bimetallic nanocrystal was found to produce a lower-wavenumber CO band ($\sim$2050 cm^{-1}), which exhibited a clear trend of shift towards that for the Pt-atop CO band as Pt concentration increases. For higher concentrations of Au, this band is strong and broad. This observation is indicative of a unique synergistic surface property in which the Pt-atop CO adsorption is greatly favored over the Au-atop CO adsorption. The complete disappearance of the Au–CO band for samples with a concentration below 65% Au does not necessarily imply the absence of Au on the surface of the nanoparticles; it implies rather the preferential Pt-atop CO adsorption over Au-atop CO adsorption, which is supported by the DFT calculation results [107]. The observation of the maximum mass activity for electrocatalytic methanol oxidation reaction under alkaline conditions around the composition of 65–85% Au coincides remarkably with the finding of the composition of $\sim$65% Au for the transition of the band features for CO adsorption, suggesting a synergistic effect of the surface reactivity for Pt atoms surrounded by Au atoms. The bimetallic Au–Pt nanoparticles (2–4 nm) form a single-phase alloy and the alloyed nanoparticle catalysts exhibit a synergistic activity in which Au surrounding Pt provides effective sites for adsorbates (CO_{ad}, OH_{ad}) in the electrocatalytic reactions.

The question whether the AuPt alloy nanoparticles exhibit a synergistic effect is addressed by studying the activity-composition correlation of MOR and ORR [31]. Considering recent modeling results for CO adsorption on small clusters of AuPt [107, 108] in which the adsorption energy is found to increase with Pt% with a maximum at $\sim$30% Pt for adsorption on Au atoms, and the FTIR results for CO adsorption of AuPt nanoparticles [39, 41], the Au atoms surrounding Pt atoms in the AuPt alloy are believed to have played an important role in either removing the intermediate CO-like species and/or providing oxygenated species in the methanol oxidation process. This assessment is consistent with the known facts that the nanoscale Au is highly active for CO oxidation [25, 109], and produces surface oxygenated species in basic electrolytes [110]. The bifunctional activity in the alkaline electrolyte involves the participation of CO and OH adsorption on Au sites in the catalytic reaction of Pt in the alloy via a combination of reaction steps (see figure 13(A)) including: the adsorption of MeOH on Pt followed by dehydrogenation; the formation of intermediate CO_{ad}/Pt; the transfer of CO_{ad}/Pt to neighboring Au-atop sites forming CO_{ad}/Au, which is supported by the favorable adsorption of CO on Au nanoparticles known from both experimental measurements [25, 109] and theoretical calculations [107, 108]; the formation of OH_{ad}/Au or surface oxides on gold, which was in fact proposed in an earlier incipient hydrous oxide/adatom mediator model [110a] and is indicated in our *in situ* measurement of the interfacial mass change accompanying the electrocatalytic oxidation of methanol on Au nanoparticle surfaces [110b]; and the reactions of Pt–CO_{ad} + Au–OH_{ad} and Au–CO_{ad} + Au–OH_{ad} towards the final product (CO_3^-).

On the basis of the ORR data in quantitatively comparing the mass activities of AuPt/C catalysts of different composition in alkaline and acidic electrolytes [31a], the mass activities were found to be strongly dependent on the bimetallic composition in the alkaline electrolyte by displaying a maximum in the region of 60–80% Au, which is higher than Pt/C and Au/C by a factor of 2–3. While the mass activity in acidic electrolyte could reflect a collective effect of the activity of Au and Pt, the concurrence of a maximized activity in the 60–80% Au composition in the alkaline electrolyte suggests a remarkable synergistic effect. An optimal fraction of Au atoms surrounding Pt could have played an important role in functioning as the sites for chemisorbed OH_{ad}^- for the dissociative adsorption of O_2 via interaction with OH_{ad}^- or for chemisorption of the reaction intermediate HO_{2ad}^- [111] (see figure 13(B)). In addition to reducing −OH on Pt by alloying Au, similarly to the process recently revealed for M_xPt_{1-x}/Pd(111) [43] and Pt/M(111) [112], the favorable chemisorption of oxygen on gold nanoparticles as evidenced by the detection of AuO^-, AuO_2^-, and AuOH on oxide-supported Au nanoparticles [113] and OH_{ad}^- on Au(110) in alkaline electrolyte [111] must have played a synergistic role. A close examination of the results for different substitution

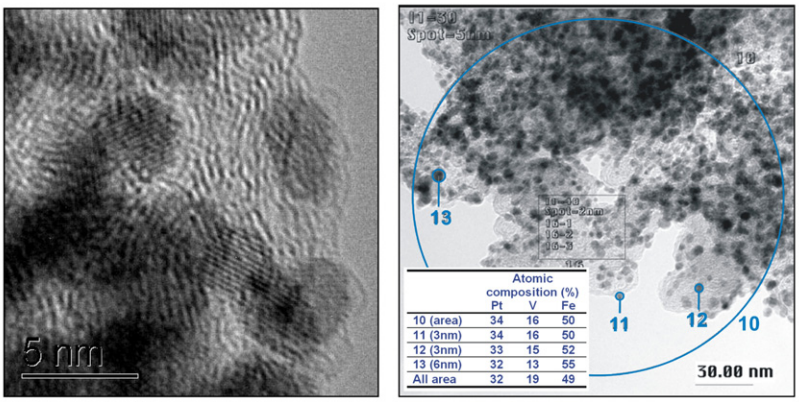

(A) (B)

Figure 14. (A) HRTEM micrograph, and (B) HRTEM–EDX data for a trimetallic nanoparticle catalyst $Pt_{33}V_{14}Fe_{53}$/C (The EDX data shown in the chart correspond to the numerically indicated particles or area in the TEM image).

in the 'organized alloy' pyramid model in the recent DFT calculation [114] reveals a minimum-featured transition of O_2-adsorption energy at 55%Au (−0.5 eV) from a relatively small variation around −1.5 eV in the 55–97% Pt region to ∼ −0.7 eV in the 0–45% Pt region. The observed maximum likely represents a compromised balance of the Pt-site activation via dissociation and the Au-site promotion by OH adsorption. The Au–OH participates in the chemisorption of the reaction intermediate from O_2 dissociation at Pt via HO^{-}_{2ad}, and such species should have sufficient binding strength with Au on further 2e reduction to H_2O on the alloy catalyst with 60–80% Au atoms surrounding Pt.

Nanoscale composition. The XRD characterization of PtVFe nanoparticles after calcination treatments revealed a typical fcc pattern with some insignificant features indicative of chemically disordered structure. The calcination treatment of the nanoparticles led to the rearrangement of Pt, V, and Fe atoms in the nanoparticles into a long-range chemically ordered fcc structure. The formation of the alloyed nanocrystalline cores is supported by the fact that the diffraction peaks of metallic platinum shift to higher angles due to lattice shrinking resulting from the doping of smaller vanadium and iron atoms. Indeed, the diffraction peak position falls in between those for the monometallic Pt and those for monometallic V and Fe. For example, the strongest peak for Pt appears at $2\theta = 40.5$, slightly higher than the Pt(111) peak ($2\theta = 39.8$) [30]. Diffraction peaks corresponding to V(110) ($2\theta = 44.7$) and Fe (110) ($2\theta = 42.2$) were not detected. The (111) peak for PtFe alloy nanoparticles ($2\theta = 41.2$ [87]) was also not detected, suggesting the absence of PtFe nanoparticles in the PtVFe nanoparticles.

The average particle sizes after the calcination treatment were found to show a slight increase (∼0.5 nm) in comparison with those before the treatment, but they displayed a highly crystalline morphology (figure 14(A)). The subtle increase in size was found to be dependent on the calcination temperature. From XRD spectra for $Pt_{32}V_{14}Fe_{54}$/C treated at 550 °C, the broad peak at low angles is from carbon-support materials. The diffraction peak positions for PtVFe fall between those for the monometallic Pt, V, and Fe [91], which indicates that these particles are largely alloyed. No secondary phase was detected. The diffraction peaks of metallic platinum shift to higher angles due to lattice shrinking resulting from the doping of smaller vanadium and iron atoms. The as-synthesized PtVFe nanoparticles were shown to be fcc structure with little chemically disordered structure [91]. After thermal treatment, there were some indications of rearrangement of Pt, V, and Fe atoms in the PtVFe nanoparticles, leading to a long-range chemically ordered fcc structure. The average sizes of the nanoparticles estimated by Scherrer correlation are slightly larger than the value determined from TEM data. The XRD data support that idea that the ternary nanoparticles are single-phase alloy. The XRD data for nanoparticles treated at different temperatures (400 and 450 °C) were also compared. The data reveal subtle differences in peak widths which can be related to differences in size change.

The question whether the nanoparticles are multimetallic in individual nanoparticles or in an ensemble of the nanoparticles was addressed using TEM–EDX (transmission electron microscopy–energy dispersive x-ray spectroscopy) [24]. TEM–EDX data (nano-composition) are also compared with DCP-AES analysis (macro-composition). By controlling the electron beam diameter and current, this measurement yielded reproducible compositions of individually isolated nanoparticles. The EDX-derived atomic composition for PtVFe nanoparticles (figure 14(B)) is found to be almost identical to DCP-AES determined composition (bulk composition), independent of the actual sizes. This finding is in contrast to the results observed from the traditional synthesis where large-sized particles are usually base metal rich and small particles are Pt-rich. Similar compositions were found for as-synthesized PtVFe nanoparticles, indicating the composition uniformity in the individual nanoparticles. Note that the effective removal of the capping molecules of the nanoparticles was evidenced by FTIR data, and the metal loading (37%) was confirmed by TGA data. Similar results were obtained for PtNiFe nanoparticles. The XRD data for PtNiFe/C showed some features indicative of chemically disordered structure before thermal treatment, but a tetragonal-type structure of PtFe type after the thermal treatment [32].

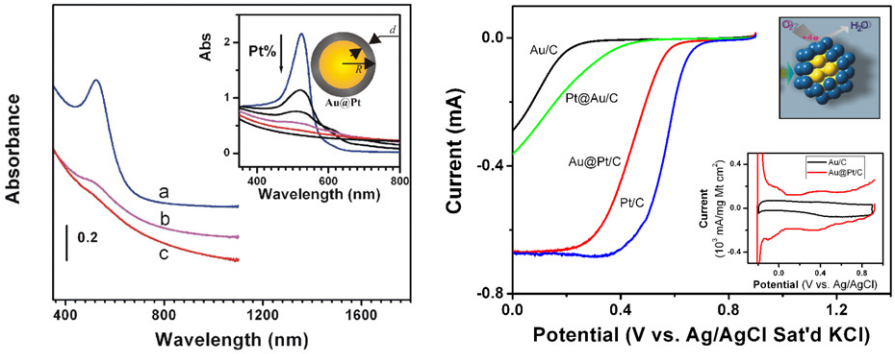

Figure 15. (A) Experiment–Mie theory comparison for the SP band for Au@Pt nanoparticles in hexane [68]. Inset: theoretical spectra as a function of shell volume fraction ($g, = 1 - (1 - d_{\text{shell}}/R_{\text{core+}shell})^3$) based on Mie theory. The two colored curves in the simulation data closely correspond to the experimental curves. (B) RDE and CV (inset) curves for the indicated catalysts in 0.5 M H_2SO_4 saturated with O_2 (metal loading 10–30%) (10 mV s^{-1}, 1600 rpm, electrode area: 0.2 cm^2).

Nanoscale core–shell structure. The importance of the relative surface alloying or layering arrangements of metals on single crystal substrates has been recognized, including the 'near surface alloy' model of a metal adlayer on a metal substrate for the oxygen reduction reaction [43, 112]. Despite the extensive studies in metal or oxide core@shell nanoparticles [115–118], relatively little is established for the correlation between the synergistic catalytic properties and the composition and spatial arrangement for metal–metal and metal–oxide core@shell nanoparticles. Built upon studies of the alloy character of bimetallic AuPt nanoparticle catalysts [29, 30], the core–shell character of Fe_3O_4@Au nanoparticles [119], and some recent theoretical insights [106–108], core@shell nanoparticles (e.g. Au@Pt, Pt@Au, Fe_3O_4@Au@Pt) have been studied to assess the nanostructural correlation of their electrocatalytic properties for MOR and ORR [68]. As revealed by the order for the increase of kinetic current and the positive-shift of the reduction potential for ORR, Au < Pt@Au < Au@Pt < Pt, the increased activity for Au@Pt catalyst is consistent with the presence of Pt on the surface [68]. The study of CO adsorption on core@shell nanoparticles (Au@Pt and Pt@Au) [68] has also revealed a resemblance of the observed CO bands at Au@Pt and Pt@Au nanoparticles to those at Pt and Au nanoparticles.

The experimental and theoretical studies of the surface plasmon (SP) resonance band of gold nanoparticles provide important information for assessing the Au@Pt nanostructure. Experimentally, the 520 nm SP band of Au core (a) is damped by the Pt shell ((b) and (c)) (figure 15(A)), which is in contrast to the SP band evolution observed for Pt@Au nanoparticles [68]. Theoretically, based on Mie theory [120] which was applied to several different core–shell nanoparticles by Mulvaney [121] and other researchers [122], the extinction cross-section C_{ext} of a small, concentric sphere is given by the coated small concentric sphere model [121].

$$C_{\text{ext}} = 4\pi R^2 k^* \,\text{Im}[(\varepsilon_{\text{shell}} - \varepsilon_{\text{m}})(\varepsilon_{\text{core}} + 2\varepsilon_{\text{shell}}) + (1-g)(\varepsilon_{\text{core}} - \varepsilon_{\text{shell}})(\varepsilon_{\text{m}} + 2\varepsilon_{\text{shell}})] \times [(\varepsilon_{\text{shell}} + 2\varepsilon_{\text{m}})(\varepsilon_{\text{core}} + 2\varepsilon_{\text{shell}}) + (1-g)(2\varepsilon_{\text{shell}} - 2\varepsilon_{\text{m}})(\varepsilon_{\text{core}} - \varepsilon_{\text{shell}})]^{-1}. \quad (7)$$

where $\varepsilon_{\text{core}}$ is the complex dielectric function of the core material, $\varepsilon_{\text{shell}}$ is for the shell, ε_{m} is the real dielectric function of the surrounding medium, g is the volume fraction of the shell layer, and R is the radius of the coated particle. From the theoretical simulation of the experimental data using the experimentally determined core and shell sizes (inset in figure 15(A)), the evolution of the SP band is quite comparable with the experimental data.

From cyclic voltammetric (CV) curves, the detection of hydrogen adsorption/desorption/evolution waves on Pt sites in acidic medium and the AuO_x oxidation/reduction waves in basic medium provided information for assessing the relative surface enrichment of Au and Pt. As shown in figure 15(B) (inset) for carbon-supported Au@Pt (A) and Au@Pt (B) nanoparticles, the detection of the hydrogen adsorption/desorption currents at $E < -0.1$ V for Au@Pt, in contrast to the absence of such waves for Au, is indicative of the presence of Pt on the nanocrystal surface, from which 43 $m^2\,g_{\text{Pt}}^{-1}$ is obtained for the ECA. For Pt@Au, the fact that the hydrogen adsorption/desorption/evolution currents are depressed, indicates the coverage of Au on the Pt nanocrystal surface. On the basis of the comparison of the RDE curves in figure 15(B) for the carbon-supported core@shell nanoparticle catalysts, the increase of kinetic current and the positive-shift of the reduction potential followed the order of Au < Pt@Au < Au@Pt < Pt. The increased activity for Au@Pt is consistent with the presence of Pt on the surface. This is also reflected by the shift of the reduction potential of Au@Pt/C from Au to Pt, and the values obtained from Levich plots for the electron transfer number (2.2 for Au, 3.9 for Pt, and 3.9 for Au@Pt). By comparing the mass activities at 0.55 V and using DCP- or TEM-determined particle size changes, 0.02, 0.09, and 0.14 mA mg_{Pt}^{-1} were estimated for Pt@Au/C, Pt/C, and Au@Pt/C, respectively.

In addition to sequential synthesis of nanoparticles with Au (or Pt) core and Pt (or Au) shells [68] or alloy structures [30], our recent work has also demonstrated the viability of temperature-controlled evolution of core–shell or phase-segregation nanostructures [51, 100]. The phase-segregation or core–shell evolution is highly dependent on the substrate and the composition of the bimetallic

nanoparticles. For example [51], phase-segregation in AuPt nanoparticles on oxide substrates has been studied *in situ* with time-resolved x-ray diffraction [51]. Silica-supported nanoparticles exhibit an alloyed structure that is preserved even after extensive annealing at temperatures as high as 700 °C. Alumina-supported nanoparticles exhibit a rich phase evolution that is sensitive to alloy composition and the details of the synthesis process. The in-depth study of this system focuses on understanding the correlation between nanostructural parameters (e.g. size and composition) and the phase properties, and developing a strategy for controlling or manipulating the degree of phase-segregation or core–shell structure formation.

5. Summary and outlook

In summary, the application of nanoscience and nanotechnology in the design, preparation, and characterization of bimetallic and trimetallic electrocatalysts is an important part of the recent progress in fuel cell catalyst research. While there are still major challenges for achieving commercially viable catalysts with high activity, high stability, and low cost, fundamental insights have been gained into the control of size, shape, composition, and phase properties of the multimetallic catalysts. It is important to emphasize that the nanoengineering approach differs from many traditional approaches to the preparation of supported catalysts in the enhanced abilities to control the particle size, shape, composition, phase, and surface properties. The facts that the bimetallic AuPt nanoparticle system displays a single-phase character different from the miscibility gap known for its bulk-scale counterpart and that phase-segregated or core–shell nanostructured bimetallic particles can be formed serve as important indications of the nanoscale manipulation of the phase properties of the catalysts. This finding and other related observations are being exploited for refining the design and preparation of various bimetallic or trimetallic catalysts. In particular, the insight gained from probing how the interactions between the nanoparticles and the planar substrate dictate the size evolution in the activation process serves as an important guiding principle for the design and control of different nanoparticle-support combinations. More importantly, the fact that some of the nanoengineered multimetallic nanoparticle catalysts exhibit electrocatalytic activities for fuel cell reactions which are four–five times higher than pure Pt catalysts constitutes the basis for further exploration of a variety of multimetallic combinations, such as $M1_nM2_{100-n}$, $M1_nM2_mM3_{100-n-m}$, and M1@M2, where M (1 or 2) = Pt, Co, Ni, V, Fe, Cu, Pd, W, Ag, Au etc), which has been part of the focal point of our continuing investigations.

An overview of the current status and future directions indicates that significant progress has been made in many areas of fundamental research into fuel cell engineering of nanostructured catalysts and the ultimate commercialization of fuel cells looks promising. However, the realization of this optimistic view has still to address challenges in several important areas. One of the most important areas is the need for a balanced and integrated approach to both fundamental and engineering aspects of the research and development of the catalysts. Fundamental investigations into the electronic and lattice structures of well-defined single crystal surfaces or selected bimetallic nanocrystals, and their characteristics such as lattice shrinking, skin effect, d-band vacancy, and so on, have generated valuable information for defining catalyst design parameters in order to achieve the highest electrocatalytic activity for fuel cell reactions. However, insights from the well-defined single crystal systems are often subject to complications when dealing with practical evaluation of the catalysts where a balance of activity and stability is essential. On the other hand, research and development in fuel cell engineering has enriched the database for assessing the optimal performance of catalysts in terms of cell voltage, power density, durability, and cost. Such a database is very useful for implementing practical applications of the catalysts, but current efforts have provided limited feedback to help with the refinement of the catalyst design parameters. This situation is largely because of the lack of understanding of the detailed structures and degradation mechanisms of the catalysts in the membrane electrode assembly under fuel cell operation conditions. As already discussed in the recent report addressing some of the current challenges [24, 65], part of the future research on catalyst design will show an increased effort that focuses on optimizing the alloy compositions toward an optimal balance of catalytic activity and stability. In addition to combinatorial screening of bimetallic or trimetallic compositions from a more engineering perspective, the fundamental insights into the control of nanoscale alloy and phase-segregation or core–shell structures, as discussed for selected example systems in this review, will help scientists and engineers to identify combinations of multimetallic compositions and phase properties with an optimized balance of catalytic activity and stability.

In another area closely related to the control of nanoscale alloys and phase-segregation, the expansion of our understanding of size, shape, composition, and lattice evolution of nanoparticles on powdery support materials under various thermal or chemical treatment conditions to a wide range of multimetallic catalyst systems will be another focal point of future research in nanostructured catalysts. As described in this review, the study of the thermal evolution of nanoparticles supported on atomically flat substrates indicates that the particle–substrate interaction is very important in addition to the particle–particle interaction. How this understanding translates to thermal evolution for nanoparticles supported on highly curved surfaces (e.g. powdery carbon black or carbon nanotube materials) is clearly an important subject area of future research for two obvious reasons. The first is the difference in mobility and adhesion of supported nanoparticles between highly curved or stepped surfaces and atomically flat surfaces. The other is the complication in probing the surface mobility or adhesion on powdery surfaces in comparison with those on flat surfaces. This is especially true because there are additional complex interactions arising from direct contact of the particle-loaded support powders that probably increase the propensity of interparticle sintering comparing to that for isolated particles on the surface. This type of interaction could also have an impact on the

phase behavior of the catalysts. The rapid development of surface techniques in probing nanoscale structures and properties, especially in *in situ* techniques (e.g. *in situ* x-ray diffraction [51] and absorption techniques [123]), is expected to advance our abilities to probe the detailed evolution of size, shape, composition, and lattice structure for multimetallic nanoparticles supported on carbon or other powdery materials under thermal, chemical, and electrochemical processes.

Addressing both fundamental and engineering issues in the above two areas will certainly lead to new insights for rational design and better control of nanostructured catalysts, leading to optimal performance and stability of fuel cells. In future studies, such insights will also be enriched by density functional theory computation [59, 124], fundamental electrochemical characterization of the electrocatalytic activity of the catalysts for fuel cell reactions under different conditions, and the evaluation of durability and degradation mechanisms of catalysts in fuel cells [125]. Such an integrated and balanced approach to the fundamental and engineering research into catalysts will serve as an effective vehicle for identifying low-cost, active, and robust catalysts for the ultimate commercialization of fuel cells.

Acknowledgments

The authors express their gratitude to former and current members of the Zhong Research Group and our collaborators who have made contributions in the last few years to the work described in this review. The research work was supported by the National Science Foundation (CBET-0709113 and CHE-0838701, CHE 0316322), ACS Petroleum Research Funds, NYSTAR, the World Gold Council, Honda, DOE SBIR, NSC Technology and other industrial Corporation contracts.

References

[1] Zhong C J, Luo J, Njoki P N, Mott D, Wanjala B, Loukrakpam R, Lim S, Wang L, Fang B and Xu Z 2008 *Energy Environ. Sci.* **1** 454–66
[2] O'hayre R, Cha S-W, Colella W and Prinz F B 2006 *Fuel Cell Fundamentals* (New York: Wiley)
[3] Chu D and Jiang R 2002 *Solid State Ion.* **148** 591–9
[4] Stone H 2005 Economic analysis of stationary PEMFC systems *DOE Hydrogen Program FY 2005 Progress Report 961* (Columbus, OH: Battelle Memorial Institute)
[5] Shukla A K and Raman R K 2003 *Annu. Rev. Mater. Res.* **33** 155–68
[6] Mehta V and Cooper J S 2003 *J. Power Sources* **114** 32
Scholta J, Kabza A, Jorissen L and Garche J 2000 *Battery Power Prod. Technol.* **4** 21
Ren X M, Zelenay P, Thomas S, Davey J and Gottesfeld S 2000 *J. Power Sources* **86** 111
[7] Spendelow J S and Wieckowski A 2004 *Phys. Chem. Chem. Phys.* **6** 5094
Bonnemann H and Nagabhushana K S 2004 *J. New Mater. Electrochem. Syst.* **7** 93
Litster S and McLean G 2004 *J. Power Sources* **130** 61
[8] Shukla A K and Raman R K 2003 *Annu. Rev. Mater. Res.* **33** 155
Adler S B 2004 *Chem. Rev.* **104** 4791
[9] Brandon N P, Skinner S and Steele B C H 2003 *Annu. Rev. Mater. Res.* **33** 183–213
Russell A E and Rose A 2004 *Chem. Rev.* **104** 4613
[10] Acres G J K, Frost J C, Hards G A, Potter R J, Ralph T R, Thompsett D, Burstein G T and Hutchings G J 1997 *Catal. Today* **38** 393
Wasmus S and Kuever A 1999 *J. Electroanal. Chem.* **461** 14
[11] Lu G Q and Wieckowski A 2000 *Curr. Opin. Colloid Interface Sci.* **5** 95
Roucoux A, Schulz J and Patin H 2002 *Chem. Rev.* **102** 3757
[12] Long J W, Stroud R M, Swider-Lyons K E and Rolison D R 2000 *J. Phys. Chem.* B **104** 9772
Ley K L, Liu R X, Pu C, Fan Q B, Leyarovska N, Segre C and Smotkin E S 1997 *J. Electrochem. Soc.* **144** 1543
[13] Lee S A, Park K W, Choi J H, Kwon B K and Sung Y E 2002 *J. Electrochem. Soc.* **149** A1299
[14] Collman J P, Bencosme C S, Durand R R, Kreh R P and Anson F C 1983 *J. Am. Chem. Soc.* **105** 2699
[15] Paulus U A, Wokaun A, Scherer G G, Schmidt T J, Stamenkovic V, Radmilovic V, Markovic N M and Ross P N 2002 *J. Phys. Chem.* B **106** 4181
[16] Casado-Rivera E, Volpe D J, Alden L, Lind C, Downie C, Vazquez-Alvarez T, Angelo A C D, DiSalvo F J and Abruna H D 2004 *J. Am. Chem. Soc.* **126** 4043
Alden L A, Han D K, Matsumoto F, Abruna H D and DiSalvo F J 2006 *Chem. Mater.* **18** 5591–6
[17a] Zhang J L, Vukmirovic M B, Xu Y, Mavrikakis M and Adzic R R 2005 *Angew. Chem. Int. Edn* **44** 2132
[17b] Sasaki K, Wang J X, Balasubramanian M, McBreen J, Uribe F and Adzic R R 2004 *Electrochim. Acta* **49** 3873
[18] Mallouk T E and Smotkin E S 2003 Combinatorial catalyst development methods *Handbook of Fuel Cells—Fundamentals, Technology and Application* ed W Vielstich, A Lamm and H A Gasteiger (New York: Wiley) p 334
[19] Sun Y, Buck H and Mallouk T E 2001 *Anal. Chem.* **73** 1599
Chen G, Delafuente D A, Sarangapani S and Mallouk T E 2001 *Catal. Today* **67** 341
Chan B C, Liu R X, Jambunathan K, Zhang H, Chen G Y, Mallouk T E and Smotkin E S 2005 *J. Electrochem. Soc.* **152** A594
[20] Liu R and Smotkin E S 2002 *J. Electroanal. Chem.* **535** 49
[21] Strasser P, Fan Q, Devenney M, Weinberg W H, Liu P and Nørskov J K 2003 *J. Phys. Chem.* B **107** 11013
[22] Guerin S, Hayden B E, Lee C E, Mormiche C, Owen J R and Russell A E 2004 *J. Comb. Chem.* **6** 149
[23] Fernandez J L, Walsh D A and Bard A J 2005 *J. Am. Chem. Soc.* **127** 357
[24] He T, Kreidler E, Xiong L, Luo J and Zhong C J 2006 *J. Electrochem. Soc.* **153** A1637
[25] Haruta M and Date M 2001 *Appl. Catal.* A **222** 427
Bismas P C, Nodasaka Y, Enyo M and Haruta M 1995 *J. Electroanal. Chem.* **381** 167
Haruta M 2004 *J. New Mater. Electrochem. Syst.* **7** 163
Haruta M 2004 *Gold Bull.* **37** 27
[26] Valden M, Lai X and Goodman D W 1998 *Science* **281** 1647
Chen M S and Goodman D W 2004 *Science* **306** 252
Campbell C T 2004 *Science* **306** 234
[27] Bond G C and Thompson D T 1999 *Catal. Rev.* **41** 319
Bond G C 2002 *Catal. Today* **72** 5
Davis R J 2003 *Science* **301** 926
Rolison D R 2003 *Science* **299** 1698
[28] Luo J, Maye M M, Kariuki N N, Wang L, Njoki P, Lin Y, Schadt M, Naslund H R and Zhong C J 2005 *Catal. Today* **99** 291
Maye M M, Kariuki N N, Luo J, Han L, Njoki P, Wang L, Lin Y, Naslunda H R and Zhong C J 2004 *Gold Bull.* **37** 217
[29] Kariuki N N, Luo J, Maye M M, Hassan S A, Menard T, Naslund H R, Lin Y, Wang C, Engelhard M H and Zhong C J 2004 *Langmuir* **20** 11240
Njoki P N, Luo J, Wang L, Maye M M, Quaizar H and Zhong C J 2005 *Langmuir* **21** 1623
[30] Luo J, Maye M M, Petkov V, Kariuki N N, Wang L, Njoki P, Mott D, Lin Y and Zhong C J 2005 *Chem. Mater.* **17** 3086
[31a] Luo J, Njoki P, Lin Y, Wang L, Mott D and Zhong C J 2006 *Electrochem. Commun.* **8** 581

[31b] Luo J, Njoki P, Lin Y, Mott D, Wang L and Zhong C J 2006 *Langmuir* **22** 2892

[32] Luo J, Kariuki N, Han L, Wang L, Zhong C J and He T 2006 *Electrochim. Acta* **51** 4821
Luo J, Wang L, Mott D, Njoki P, Kariuki N, Zhong C J and He T 2006 *J. Mater. Chem.* **16** 1665

[33] Bonnemann H and Nagabhushana K S 2004 *J. New Mater. Electrochem. Syst.* **7** 93
Brandon N P, Skinner S and Steele B C H 2003 *Annu. Rev. Mater. Res.* **33** 183

[34] Zhong C J, Luo J, Maye M M, Han L, Kariuki N and He T 2006 *US Patent Specification* 7,053,021

[35] He T, Zhong C J, Luo J, Han L, Maye M M, Kariuki N and Wang L 2008 *US Patent Specification* 7,335,245

[36] Zhong C J, Luo J, Maye M M and Kariuki N 2007 *US Patent Specification* 7,208,439

[37] Wang L Y, Park H-Y, Lim S I, Schadt M J, Mott D, Luo J, Wang X and Zhong C J 2008 *J. Mater. Chem.* **18** 2629

[38] Haruta M 2005 *Nature* **437** 1098

[39] Mott D, Luo J, Njoki P N, Lin Y, Wang L Y and Zhong C J 2007 *Catal. Today* **122** 378

[40] Ponec V and Bond G C 1995 *Catalysis by Metals and Alloys* (Amsterdam: Elsevier)

[41] Mott D, Luo J, Smith A, Njoki P N, Wang L and Zhong C J 2007 *Nanoscale Res. Lett.* **2** 12

[42] Zhang J, Sasaki K, Sutter E and Adzic R R 2007 *Science* **315** 220

[43] Zhang J, Vukmirovic M B, Sasaki K, Nilekar A U, Mavrikakis M and Adzic R R 2005 *J. Am. Chem. Soc.* **127** 12480

[44] Van Brussel M, Kokkinidis G, Vandendael I and Buess-Herman C 2002 *Electrochem. Commun.* **4** 808
El-Deab M S and Ohsaka T 2003 *J. Electroanal. Chem.* **553** 107

[45] El-Deab M S and Ohsaka T 2002 *Electrochim. Acta* **47** 4255

[46] *Gold 2003: New Industrial Applications for Gold* 2003 (London: World Gold Council) proceeding volume

[47] Kim Y D, Fischer M and Gantefor G 2003 *Chem. Phys. Lett.* **377** 170
Xu Y and Mavrikakis M 2003 *J. Phys. Chem.* B **107** 9298

[48] Hernandez-Fernandez P, Rojas S, Ocon P, Gomez J L, Fabian J S, Sanza J, Pena M A, Garcia-Garcia F J, Terreros P and Fierro J L G 2007 *J. Phys. Chem.* C **111** 2913

[49] Selvarani G, Selvaganesh S V, Krishnamurthy S, Kirithika G V M, Sridhar P, Pitchumani S and Shukla A K 2009 *J. Phys. Chem.* C **113** 7461

[50] Kumar S S and Phani K L N 2009 *J. Power Sources* **187** 19

[51] Malis O, Radu M, Mott D, Wanjala B, Luo J and Zhong C J 2009 *Nanotechnology* **20** 245708

[52] Manthiram A, Murugan A V, Sarkar A and Muraliganth T 2008 *Energy Environ. Sci.* **1** 621–38

[53] Spendelow J S and Wieckowski A 2007 *Phys. Chem. Chem. Phys.* **9** 2654–75
Maillard F, Lu G Q, Wieckowski A and Stimming U 2005 *J. Phys. Chem.* B **109** 16230–43

[54] Antolini E 2004 *J. Appl. Electrochem.* **34** 563–76

[55] Yamamoto K, Imaoka T, Chun W J, Enoki O, Katoh H, Takenaga M and Sonoi A 2009 *Nat. Chem.* **1** 397–402

[56] Stamenkovic V R, Mun B S, Arenz M, Mayrhofer K J J, Lucas C A, Wang G F, Ross P N and Markovic N M 2007 *Nat. Mater.* **6** 241–7

[57] Markovic N M and Ross P N 2002 *Surf. Sci. Rep.* **45** 121–229

[58] Strmcnik D, Kodama K, van der Vliet D, Greeley J, Stamenkovic V R and Markovic N M 2009 *Nat. Chem.* **1** 466–72

[59] Greeley J, Stephens I E L, Bondarenko A S, Johansson T P, Hansen H A, Jaramillo T F, Rossmeisl J, Chorkendorff I and Norskov J K 2009 *Nat. Chem.* **1** 552–6

[60] Chen S, Sheng W, Yabuuchi N, Ferreira P J, Allard L F and Shao-Horn Y 2009 *J. Phys. Chem.* C **113** 1109–25

[61] Koh S, Toney M F and Strasser P 2007 *Electrochim. Acta* **52** 2765–74

[62] Koh S, Yu C, Mani P, Srivastava R and Strasser P 2007 *J. Power Sources* **172** 50–6

[63] Schulenburg H, Muller E, Khelashvili G, Roser T, Bonnemann H, Wokaun A and Scherer G G 2009 *J. Phys. Chem.* C **113** 4069–77

[64] Bezerra C W B, Zhang L, Liu H, Lee K, Marques A L B, Marques E P, Wang H and Zhang J 2007 *J. Power Sources* **173** 891–908

[65] He T, Kreidler E, Xiong L F and Ding E R 2007 *J. Power Sources* **165** 87–91

[66] Antolini E, Passos R R and Ticianelli E A 2002 *Electrochim. Acta* **48** 263–70

[67] Gasteiger H A, Kocha S S, Sompalli B and Wagner F T 2005 *Appl. Catal.* B **56** 9

[68] Luo J, Wang L, Mott D, Njoki P, Lin Y, He T, Xu Z, Wanjana B, Lim I-I S and Zhong C J 2008 *Adv. Mater.* **20** 4342–7

[69] Klabunde K J 2001 *Nanoscale Materials in Chemistry* (New York: Wiley)

[70] Antolini E 2003 *Mater. Chem. Phys.* **78** 563
Rao C R K and Trivedi D C 2005 *Coord. Chem. Rev.* **249** 613

[71] Yang H, Vogel W, Lamy C and Alonso-Vante N 2004 *J. Phys. Chem.* B **108** 11024

[72] Feldheim D L and Foss C A Jr 2002 *Metal Nanoparticles: Synthesis, Characterization, and Applications* (New York: Dekker)

[73] Waszczuk P, Lu G Q, Wieckowski A, Lu C, Rice C and Masel R I 2002 *Electrochim. Acta* **47** 3637
Park K W, Choi J H, Kwon B K, Lee S A, Sung Y E, Ha H Y, Hong S A, Kim H and Wieckowski A 2002 *J. Phys. Chem.* B **106** 1869

[74] Schmidt T J, Gasteiger H A and Behm R J 1999 *Electrochem. Commun.* **1** 1

[75] Raja R, Khimyak T, Thomas J M, Hermans S and Johnson B F G 2001 *Angew. Chem. Int. Edn* **40** 4638
Jones F E, Milne S B, Gurau B, Smotkin E S, Stock S R and Lukehart C M 2002 *J. Nanosci. Nanotechnol.* **2** 81
Dickinson A J, Carrette L P L, Collins J A, Friedrich K A and Stimming U 2002 *Electrochim. Acta* **47** 3733

[76] Zhong C J and Maye M M 2001 *Adv. Mater.* **13** 1507

[77] Crown A, Kim H, Lu G Q, de Moraes I R, Rice C and Wieckowski A 2000 *J. New Mater. Electrochem. Syst.* **3** 275
Aiken J D III and Finke R G 1999 *J. Mol. Catal.* A **145** 1

[78] Li H, Luk Y-Y and Mrksich M 1999 *Langmuir* **15** 4957
Ingram R S and Murray R W 1998 *Langmuir* **14** 4115

[79] Peng X, Schlamp M C, Kadavanich A V and Alivisatos A P 1997 *J. Am. Chem. Soc.* **119** 7019
Oldenburg S J, Averitt R D, Westcott S L and Halas N J 1998 *Chem. Phys. Lett.* **288** 243

[80] Galow T H, Drechsler U, Hanson J A and Rotello V M 2002 *Chem. Commun.* 1076

[81] Brust M, Walker M, Bethell D, Schiffrin D J and Whyman R 1994 *J. Chem. Soc., Chem. Commun.* 801
Templeton A C, Wuelfing W P and Murray R W 2000 *Acc. Chem. Res.* **33** 27

[82a] Schmid G, Maihack V, Lantermann F and Peschel S 1996 *J. Chem. Soc., Dalton Trans.* 589

[82b] Paulus U A, Endruschat U, Feldmeyer G J, Schmidt T J, Bonnemann H and Behm R J 2000 *J. Catal.* **195** 383

[83] Whetten R L, Khoury J T, Alvarez M M, Murthy S, Vezmar I, Wang Z L, Stephens P W, Cleveland C L, Luedtke W D and Landman U 1996 *Adv. Mater.* **8** 428

[84] El-Sayed M A 2001 *Acc. Chem. Res.* **34** 257
Kiely C J, Fink J, Zheng J G, Brust M, Bethell D and Schiffrin D J 2000 *Adv. Mater.* **12** 640

[85] Caruso F 2001 *Adv. Mater.* **13** 11 and references therein
Schneider J J 2001 *Adv. Mater.* **13** 529
Schärtl W 2000 *Adv. Mater.* **12** 1899

[86] Storhoff J J and Mirkin C 1999 *Chem. Rev.* **99** 1849
Mbindyo J K N, Reiss B D, Martin B R, Keating C D, Natan M J and Mallouk T E 2001 *Adv. Mater.* **13** 249
Crooks R M, Zhao M Q, Sun L, Chechik V and Yeung L K 2001 *Acc. Chem. Res.* **34** 181

[87] Sun S H, Murray C B, Weller D, Folks L and Moser A 2000 *Science* **287** 1989
Sun S H, Fullerton E E, Weller D and Murray C B 2001 *IEEE Trans. Magn.* **37** 1239

[88] Chen M and Nikles D E 2002 *Nano Lett.* **2** 211

[89] Han L, Wu W, Kirk F L, Luo J, Maye M M, Kariuki N, Lin Y, Wang C and Zhong C J 2004 *Langmuir* **20** 6019

[90] Hostetler M J, Zhong C J, Yen B K H, Anderegg J, Gross S M, Evans N D, Porter M D and Murray R W 1998 *J. Am. Chem. Soc.* **120** 9396

[91] Luo J, Han L, Kariuki N N, Wang L, Mott D, Zhong C J and He T 2005 *Chem. Mater.* **17** 5282

[92a] Luo J, Jones V W, Maye M M, Han L, Kariuki N N and Zhong C J 2002 *J. Am. Chem. Soc.* **124** 13988

[92b] Maye M M, Luo J, Han L, Kariuki N and Zhong C J 2003 *Gold Bull.* **36** 75

[92c] Luo J, Maye M M, Han L, Kariuki N, Jones V W, Lin Y, Engelhard M H and Zhong C J 2004 *Langmuir* **20** 4254

[92d] Luo J, Jones V W, Han L, Maye M M, Kariuki N and Zhong C J 2004 *J. Phys. Chem.* B **108** 9669

[93a] Maye M M, Lou Y and Zhong C J 2000 *Langmuir* **16** 7520

[93b] Lou Y, Maye M M, Han L, Luo J and Zhong C J 2001 *Chem. Commun.* 473

[93c] Luo J, Lou Y B, Maye M M, Zhong C J and Hepel M 2001 *Electrochem. Commun.* **3** 172

[93d] Luo J, Maye M M, Lou Y, Han L, Hepel M and Zhong C J 2002 *Catal. Today* **77** 127

[93e] Maye M M, Luo J, Lin Y, Engelhard M H, Hepel M and Zhong C J 2003 *Langmuir* **19** 125

[93f] Kariuki N N, Luo J, Han L, Maye M M, Moussa L, Patterson M, Lin Y, Engelhard M H and Zhong C J 2004 *Electroanalysis* **16** 120

[94] Rajesh B, Karthik V, Karthikeyan S, Thampi K R, Bonard J-M and Viswanathan B 2002 *Fuel* **81** 2177
Wu H Q, Wei X W, Shao M W, Gu J S and Qu M Z 2002 *J. Mater. Chem.* **12** 1919
Gao X P, Lan Y, Pan G L, Wu F, Qu J Q, Song D Y and Shen P W 2001 *Electrochem. Solid State Lett.* **4** A173
Frackowiak E and Beguin F 2002 *Carbon* **40** 1775

[95] Che G L, Lakshmi B B, Fisher E R and Martin C R 1998 *Nature* **393** 346
Shao Y, Kou R, Wang J, Wang C, Viswanathan V, Liu J, Wang Y and Lin Y 2009 *J. Nanosci. Nanotechnol.* **9** 5811–5

[96] Nashner M S, Frenkel A I, Somerville D, Hills C W, Shapley J R and Nuzzo R G 1998 *J. Am. Chem. Soc.* **120** 8093

[97] Wuelfing W P, Zamborini F P, Templeton A C, Wen X G , Yoon H and Murray R W 2001 *Chem. Mater.* **13** 87

[98a] Nakaso K, Shimada M, Okuyama K and Deppert K 2002 *J. Aerosol Sci.* **33** 1061

[98b] Mitchell C E J, Howard A, Carney M and Egdell R G 2001 *Surf. Sci.* **490** 196

[98c] Weber A P and Friedlander S K 1997 *J. Aerosol Sci.* **28** 179

[99] Campbell C T, Parker S C and Starr D E 2002 *Science* **298** 811

[100] Wanjala B, Fang B, Luo J and Zhong C J manuscript in preparation
Zhong C J *et al* 2009 *Materials Research Society Mtg (Boston, Nov–Dec 2009)* T9.6
Loukrakpam R *et al* 2009 *Materials Research Society Mtg (Boston, Nov–Dec 2009)* Y8.20
Wanjala B *et al* 2009 *Materials Research Society Mtg (Boston, Nov–Dec 2009)* Y8.21

[101] Fang B, Luo J, Njoki P N, Loukrakpam R, Mott D, Wanjala B, Hu X and Zhong C J 2009 *Electrochem. Commun.* **11** 1139–41
Fang B, Luo J, Njoki P N, Loukrakpam R, Wanjala B, Hu X and Zhong C J 2009 *Electrochim. Acta* submitted

[102] Hostetler M J *et al* 1998 *Langmuir* **14** 17
Shon Y S, Gross S M, Dawson B, Porter M and Murray R W 2000 *Langmuir* **16** 6555

[103] Sun L and Crooks R M 2002 *Langmuir* **18** 8231

[104] Takano H, Kenseth J R, Wong S-S, O'Brien J C and Porter M D 1999 *Chem. Rev.* **99** 2845

[105] Maye M M, Luo J, Han L and Zhong C J 2001 *Nano Lett.* **1** 575–80
Wang L, Luo J, Schadt M J and Zhong C J 2009 *Langmuir* (doi:10.1021/la901811g)

[106] Xiao S, Hu W, Luo W, Wu Y, Li X and Deng H 2006 *Eur. Phys. J.* B **54** 479

[107] Pedersen M Ø, Helveg S, Ruban A, Stensgaard I, Lægsgaard E, Nørskov J K and Besenbacher F 1999 *Surf. Sci.* **426** 395

[108] Song C, Ge Q and Wang L 2005 *J. Phys. Chem.* B **109** 22341
Ge Q, Song C and Wang L 2006 *Comput. Mater. Sci.* **35** 247

[109] Haruta M 1997 *Catal. Today* **36** 153
Haruta M 2005 *Nature* **437** 1098

[110a] Burke L D 2004 *Gold Bull.* **37** 125

[110b] Luo J, Maye M M, Han L, Zhong C J and Hepel M 2002 *J. New Mater. Electrochem. Syst.* **5** 237

[111] Strbac S and Adzic R R 1996 *J. Electroanal. Chem.* **403** 169

[112] Zhang J, Vukmirovic M B, Xu Y, Mavrikakis M and Adzic R R 2005 *Angew. Chem. Int. Edn* **44** 2132

[113] Fu L, Wu N Q, Yang J H, Qu F, Johnson D L, Kung M C, Kung H H and Dravid V P 2005 *J. Phys. Chem.* B **109** 3704

[114] Tielens F, Andres J, Van Brussel M, Buess-Hermann C and Geerlings P 2005 *J. Phys. Chem.* B **109** 7624

[115] Garcia-Gutierrez D I, Gutierrez-Wing C E, Giovanetti L, Ramallo-Lopez J M, Requejo F G and Jose-Yacaman M 2005 *J. Phys. Chem.* B **109** 3813

[116] Damle C, Biswas K and Sastry M 2001 *Langmuir* **17** 7156
Toshima N, Kanemaru M, Shiraishi Y and Koga Y 2005 *J. Phys. Chem.* B **109** 16326

[117] Teng X W, Black D, Watkins N J, Gao Y L and Yang H 2003 *Nano Lett.* **3** 261
Zeng H, Li J, Wang Z L, Liu J P and Sun S H 2004 *Nano Lett.* **4** 187
Xu Z, Hou Y and Sun S 2007 *J. Am. Chem. Soc.* **129** 8698

[118] Toshima N, Shiraishi Y, Shiotsuki A, Ikenaga D and Wang Y 2001 *Eur. Phys. J.* D **16** 209
Park J I, Kim M G, Jun Y W, Lee J S, Lee W R and Cheon J 2004 *J. Am. Chem. Soc.* **126** 9072

[119] Wang L, Luo J, Fan Q, Suzuki M, Suzuki I S, Engelhard M H, Lin Y, Kim N, Wang J Q and Zhong C J 2005 *J. Phys. Chem.* B **109** 21593
Wang L, Luo J, Maye M M, Fan Q, Rendeng Q, Engelhard M H, Wang C, Lin Y and Zhong C J 2005 *J. Mater. Chem.* **15** 1821
Park H Y, Schadt M J, Wang L, Lim I-I S, Njoki P N, Kim S H, Jang M Y, Luo J and Zhong C J 2007 *Langmuir* **23** 9050

[120] Bohren C F and Huffman D R 1983 *Absorption and Scattering of Light by Small Particles* (New York: Wiley)

[121] Mulvaney P 1996 *Langmuir* **12** 788

[122] Reinhard B M, Siu M, Agarwal H, Alivisatos A P and Liphardt J 2005 *Nano Lett.* **5** 2246

[123] Scott F J, Mukerjee S and Ramaker D E 2007 *J. Electrochem. Soc.* **154** A396
Lewis E A, Segre C U and Smotkin E S 2009 *Electrochim. Acta* **54** 7181

[124] Dimakis N, Cowan M, Hanson G and Smotkin E S 2009 *J. Phys. Chem.* C **113** 18730

[125] Ramaswamy N, Hakim N and Mukerjee S 2008 *Electrochim. Acta* **53** 3279